

High Resolution Optical Microscopy



Wolfram Ibach, Olaf Hollricher

Copyright ©2002 **WITec GmbH**

All rights reserved

Contents

1 Theory	9
1.1 Introduction to confocal microscopy	9
1.2 Electromagnetic scattering	10
1.3 3D-Intensity distribution in the focus	12
1.3.1 Large aperture angles	12
1.3.2 Transition to small aperture angles	17
1.4 Theory of image formation	18
1.4.1 Microscope	19
1.4.2 Confocal microscope	20
1.4.3 Confocal fluorescence microscope	21
1.4.4 2-Photon-Microscope	22
1.4.5 Confocal 2-Photon-Microscope	23
1.5 Image formation for light scattering	24
1.5.1 Scattering point	24
1.5.2 Reflection at a mirror	25
1.6 Image formation for fluorescence	27
1.6.1 Fluorescing point	28
1.6.2 Fluorescing layer	29
1.7 Near-field microscopy	30
1.7.1 Dipole radiation	32

2 The Instrument	35
2.1 The microscope	35
2.2 Descriptions of the components	38
2.2.1 Data acquisition	38
2.2.2 Scan table	40
2.2.3 Detector	40
2.2.4 Setup for 2-photon excitation	41
2.2.5 Pulse compression with prechirp	42
2.2.6 Pinhole size	44
2.2.7 Near-field setup	47
3 Sample systems	51
3.1 Reflection at a mirror	51
3.2 2-photon microscopy	55
3.3 Confocal fluorescence microscopy	58
3.4 Confocal versus near-field microscopy	61
3.5 Depth resolution in confocal fluorescence microscopy	67
3.6 Imaging of a a semiconductor surface	70
3.6.1 Extended focus	71
3.6.2 Automatical focus	73
Bibliography	75

List of Figures

1.1	Principal setup of a confocal microscope	10
1.2	Imaging geometry	11
1.3	Electrical energy density in the focal plane	15
1.4	Cut through the electrical energy density	16
1.5	Full width at half maximum (FWHM) of the field distribution	18
1.6	Intensity distribution of two points that fulfil the Rayleigh criterion	20
1.7	Comparison of the intensity PSFs	21
1.8	Scattering point	24
1.9	Lateral resolution of a scattering point	25
1.10	Reflection at a mirror	26
1.11	Depth resolution for a reflecting layer	27
1.12	Lateral resolution for a fluorescing point	28
1.13	Depth resolution at a fluorescing layer	29
2.1	The instrument	37
2.2	Setup	39
2.3	Pulse compression	43
2.4	Autocorrelation	44
2.5	Collection efficiency	47
2.6	Near-Field-Objective	48
2.7	Cantilever-SNOM sensors	49

2.8 Aperture	49
2.9 Distance feedback with Cantilever-SNOM sensors	50
3.1 Wavefront error due to incorrect beam path	52
3.2 Wavefront error due to wrong cover glass thickness	53
3.3 Laterally shifted pinhole	54
3.4 Comparison with theory	55
3.5 2-photon microscopy	57
3.6 Fluorescing layer	59
3.7 Cross section through the crack in Fig. 3.6	60
3.8 Latex projection pattern	62
3.9 Confocal	64
3.10 SNOM	65
3.11 SNOM with 29nm resolution	66
3.12 Chemische Struktur von Perylentetracarbonsäurediimid	67
3.13 Perylentetracarbonsäurediimid	68
3.14 Intensity profile of Fig. 3.13	70
3.15 Scheme to calculate extended focus images	71
3.16 Extended focus of a structured semiconductor surface	72
3.17 Scheme to calculate automatical focus images	73
3.18 Automatical focus and topography of a structured semiconductor (German telephone card chip)	74

Introduction

Lucius Annaeus Seneca¹ was one of the first, who described the optical magnification of water-filled glass spheres (magnifying glass). Since this time, many researcher knew about the magnifying properties of convex lenses, but it took more than one millennium, until the Dutch optician Hans Janssen and his son Zacharias build the first microscope by combining several lenses in 1590. At the end of the 19th century, the development of the microscope was strongly pushed due to the combined work of Ernst Abbe², Carl Zeiss³ and Otto Schott⁴.

Up to now, the microscope is one of the most important tools for the investigation of objects in the micrometer scale. During the 20th century, many new imaging techniques, like e.g. phase contrast, interference microscopy and dark field illumination have been developed. One of the most important techniques in optical microscopy is fluorescence marking of objects with dyes containing functional groups. These dyes bind only at very specific parts of the sample which is very essential in medical diagnostics and science.

In the last years, the 2-photon-microscopy, which is the fluorescence excitation with half of the transition energy of the dye, tends to get its way into biology. Biological samples are much more transparent for infrared radiation than for visible light and bleaching is limited to the focal plane. Other advantages are the depth resolution and the ease to excite autofluorescence in the ultraviolet.

Despite many new imaging techniques, the optical resolution stayed nearly con-

¹Lucius Annaeus Seneca the younger (* around 4 v. Chr., † 65 n. Chr.).

²Ernst Abbe (*23.1.1840, †14.1.1905) was professor for physics in Jena (Germany) and developed the theory of the optical microscope.

³Carl Zeiss (*11.9.1816, †3.12.1888) was a precision mechanic and opened an optical workshop in Jena in 1848.

⁴Otto Schott (*17.12.1851, †27.8.1935) received a PhD in chemistry and developed several new kinds of glass for microscopy.

stant since the beginning of the 20th century. A slight increase in resolution, which is also possible in combination with the 2-photon-excitation, was achieved in the last years with confocal microscopy. In this technique, a point-like light source is focussed onto the sample and this spot is again focussed onto a point-like detector. The image is obtained by scanning either the sample or the excitation spot line by line. Besides depth resolution and a much higher image contrast, under optimum conditions also an increase in resolution of a factor $\sqrt{2}$ can be achieved.

The only technique to overcome the diffraction limit of the microscope and to achieve a substantial increase in resolution is the optical near-field microscopy. In this technique, a tiny aperture is scanned in nanometer distance across the sample. In principle, a resolution in the order of 10 nm can be achieved in the optical wavelength range. However, this resolution can be obtained only very close to the sample surface. Looking deep into the sample (like in confocal microscopy) is not possible due to the surface sensitivity of this technique.

Purpose of this tutorial is to give the reader a comprehensive overview over the field of high resolution optical microscopy.

The first chapter describes the theory of image formation in an optical microscope. Differences between various techniques like conventional, confocal, 2-photon- and near-field microscopy are explained. The next chapter describes the instrument, necessary adjustments and the choice of the appropriate pinhole diameter, suitable for highest depth and lateral resolution. In the last chapter, the resolution obtained with different imaging techniques is discussed and compared to near-field microscopy. It will be explained what has to be taken into account to achieve optimum results.

Chapter 1

Theory

All confocal imaging techniques, like e.g. the confocal fluorescence microscopy or the confocal 2-photon microscopy are based on a point to point image formation. A detailed overview over these methods can be found e.g. in the book of James B. Pawley [1].

In this chapter, the theoretical background for this technique will be explained. The electromagnetic field distribution in the focus of an objective will be calculated, which is the starting point for the mathematical description of image formation. Furthermore, the fundamental difference between confocal microscopy and confocal fluorescence microscopy with its different kinds of excitation possibilities will be discussed.

1.1 Introduction to confocal microscopy

In confocal¹ microscopy, a point-like light source is focussed with a lens or an objective onto a sample. The spacial extension of the focus spot on the sample is determined by the wavelength λ and the quality of the image formation. The image spot is then focussed through the same (or a second) lens onto an aperture (pinhole) in front of a detector. The size of the pinhole is chosen such that only the central part of the focus can pass the pinhole and reach the detector.

One can see in Fig. 1.1 that rays that do not come from the focal plane will not be

¹konfokal: (lat.) with equal focal points

able to pass the pinhole. From this simple geometrical picture, two advantages of confocal microscopy can already be seen. First of all, through scanning of the sample with respect to the objective, a three dimensional image of the sample can be obtained. This is not possible in conventional microscopy. Second, only light from the focal plane will hit the detector. Therefore, image contrast is strongly enhanced.

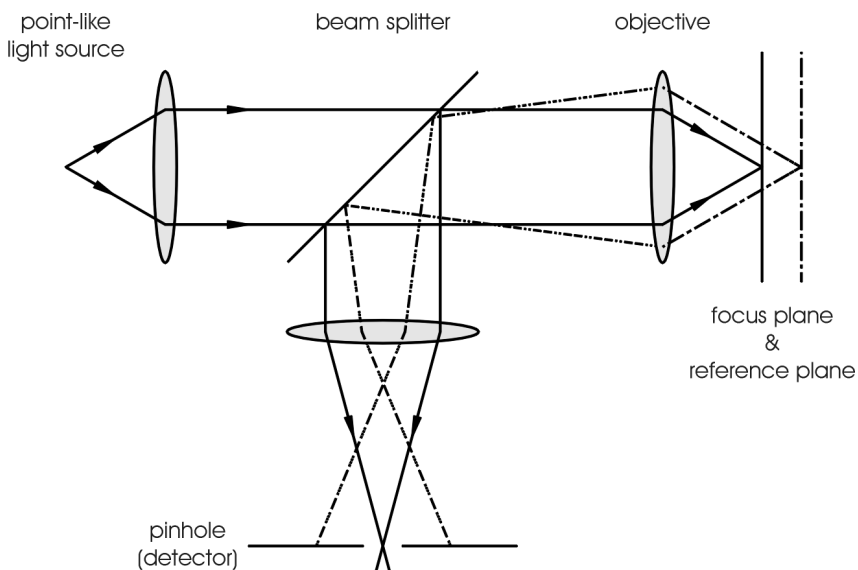


fig. 1.1: Principal setup of a confocal microscope.

As another point, by choosing an appropriate pinhole diameter the lateral resolution can be increased up to a factor of $\sqrt{2}$.

1.2 Electromagnetic scattering in optical systems

In this section, the basic ideas necessary for calculating the field distribution in the focus are provided. A detailed discussion can be found in the articles of E. Wolf [2, 3]. Fig. 1.2 shows the geometry of the setup.

S_0 is the origin of a monochromatic wave with frequency ω and S_1 its image, obtained with geometric ray optics.

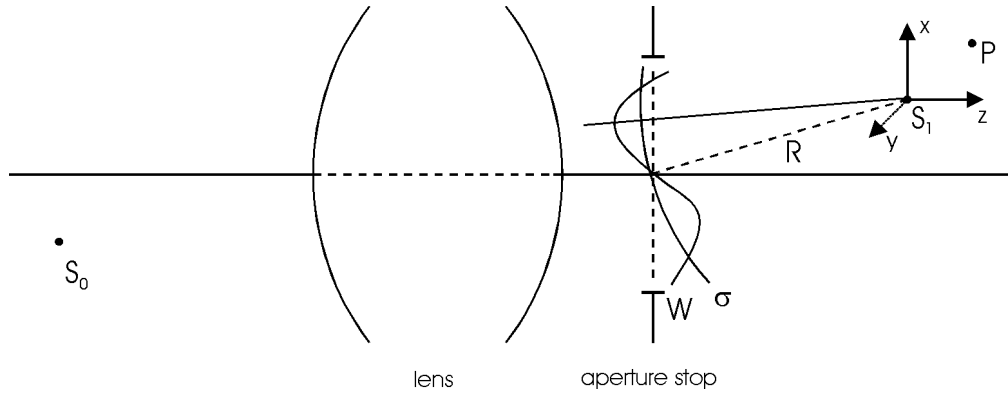


fig. 1.2: Imaging geometry.

The field distribution in the focus is described in the cartesian coordinate system with origin in S_1 . Starting point is the HELMHOLTZ-EQUATION

$$\Delta \vec{E} + k^2 \vec{E} = \vec{0} \quad ,$$

which describes the space dependent part of the electrical field.

$$\vec{E}(P, t) = \Re \left\{ \vec{e}(P) e^{-i\omega t} \right\}$$

In general, the HELMHOLTZ-EQUATION can be satisfied by

$$\vec{e}(P) = \int_{-\infty}^{\infty} \int_{-\infty}^{\infty} e^{ik(s_x x + s_y y)} \left\{ \vec{U}(s_x, s_y) e^{iks_z z} + \vec{V}(s_x, s_y) e^{-iks_z z} \right\} ds_x ds_y \quad (1.1)$$

where s_z is given by the condition $s_x^2 + s_y^2 + s_z^2 = 1$. $\vec{U}(s_x, s_y)$ and $\vec{V}(s_x, s_y)$ are arbitrary functions that have to fulfill the KIRCHHOFF BOUNDARY CONDITIONS. For the magnetic field

$$\vec{H}(P, t) = \Re \left\{ \vec{h}(P) e^{-i\omega t} \right\}$$

similar expressions can be found.

As described in Ref. [2], an approximate solution for the electrical field in the plane of the aperture can be found with the method of stationary phase. This leads to two general solutions:

$$\vec{e}(P) = -\frac{ik}{2\pi} \iint_{\Omega} \frac{\vec{a}(s_x, s_y)}{s_z} e^{ik\{\Phi(s_x, s_y) + s_x x + s_y y + s_z z\}} ds_x ds_y \quad (1.2)$$

$$\vec{h}(P) = -\frac{ik}{2\pi} \iint_{\Omega} \frac{\vec{b}(s_x, s_y)}{s_z} e^{ik\{\Phi(s_x, s_y) + s_x x + s_y y + s_z z\}} ds_x ds_y \quad (1.3)$$

Here, the functions $\vec{a}(s_x, s_y)$, $\vec{b}(s_x, s_y)$ and $\Phi(s_x, s_y)$ take the part of $\vec{U}(s_x, s_y)$ and $\vec{V}(s_x, s_y)$. These two functions have the following meaning:

The abberation function $\Phi(s_x, s_y)$ is a measure how strong the real wavefront W deviates from the ideal spherical wavefront σ . The factor $\vec{a}(s_x, s_y)$ determines the amplitude of the field. In the geometrical optic, this is the intensity of the light beam. Along every beam $\vec{a}(s_x, s_y)$ is independent of the position of the aperture.

All three numbers \vec{a} , \vec{b} and Φ can be determined by Ray-Traceing algorithms.

Equations (1.2) and (1.3) represent the addition of planar waves inside the aperture. In contrast, using the HUYGENS-FRESNEL PRINCIPLE one would add spherical waves.

1.3 3D-Intensity distribution in the focus

In literature one can find two different descriptions for the field distribution in the focus. One describes the electrical field as a scalar and is correct only for small aperture angles. The vector description from B. Richards and E. Wolf [4] is more appropriate for the nature of light. Here, the field distribution is a function of the aperture angle α , and therefore can be also applied to systems with large aperture angles. If one compares small and large aperture angles one sees that the electrical energy density in the focal plane is not radial symmetric any more, but depends on the original polarization direction. Additionally, the energy density in the secondary maxima and minima gets larger.

1.3.1 Large aperture angles

For an abberation free system ($\Phi(s_x, s_y) = 0$), that is a system without wavefront errors, all components of the electrical field in the focus can be derived from equations (1.2) and (1.3). To simplify the calculation the point S_0 (Fig. 1.2) is shifted to infinity. This point is the origin of an electrical field which is polarized in x-direction ($\phi_P = 0$). Therefore, the image of S_0 lays exactly in the focal plane of the lens S_1 . A change of the transmission of the lens due to its surface curvature, which could be calculated with the FRESNEL FORMULAS is neglected. Therefore, the surface cur-

vature of the lens has to be sufficiently small.

Because of the symmetry of the system, it is appropriate to change to spherical coordinates.

$$x = r_P \sin \theta_P \cos \phi_P, \quad y = r_P \sin \theta_P \sin \phi_P, \quad z = r_P \cos \theta_P$$

Origin of the coordinate system is the geometrical focus point S_1 . We also change to so called optical coordinates

$$\left. \begin{aligned} u &= kr_P \cos \theta_P \sin^2 \alpha &= kz \sin^2 \alpha \\ v &= kr_P \sin \theta_P \sin \alpha &= k\sqrt{x^2 + y^2} \sin \alpha \end{aligned} \right\} \quad (1.4)$$

with

$$\begin{aligned} k &= \frac{2\pi}{\lambda} && : \text{absolute value of the wave vector} \\ 0^\circ < \alpha < 90^\circ & && : \text{half of the aperture angle} \end{aligned}$$

to eliminate the wavelength dependence. With these coordinates, the spacial dependent part of the electrical and magnetically field can be written as

$$\left. \begin{aligned} e_x(u, v) &= -iA(I_0 + I_2 \cos 2\phi_P) \\ e_y(u, v) &= -iAI_2 \sin 2\phi_P \\ e_z(u, v) &= -2AI_1 \cos \phi_P \end{aligned} \right\} \quad (1.5)$$

$$\left. \begin{aligned} h_x(u, v) &= -iAI_2 \sin 2\phi_P \\ h_y(u, v) &= -iA(I_0 - I_2 \cos 2\phi_P) \\ h_z(u, v) &= -2AI_1 \sin \phi_P \end{aligned} \right\} \quad (1.6)$$

Herein, I_0 , I_1 and I_2 are defined over the integrals

$$\left. \begin{aligned} I_0(u, v) &= \int_0^{\alpha} \cos^{\frac{1}{2}} \theta \sin \theta (1 + \cos \theta) J_0 \left(\frac{v \sin \theta}{\sin \alpha} \right) e^{iu \cos \theta / \sin^2 \alpha} d\theta \\ I_1(u, v) &= \int_0^{\alpha} \cos^{\frac{1}{2}} \theta \sin^2 \theta J_1 \left(\frac{v \sin \theta}{\sin \alpha} \right) e^{iu \cos \theta / \sin^2 \alpha} d\theta \\ I_2(u, v) &= \int_0^{\alpha} \cos^{\frac{1}{2}} \theta \sin \theta (1 - \cos \theta) J_2 \left(\frac{v \sin \theta}{\sin \alpha} \right) e^{iu \cos \theta / \sin^2 \alpha} d\theta \end{aligned} \right\} \quad (1.7)$$

The parameter $A = \frac{kfl_0}{2} = \frac{\pi fl_0}{\lambda}$ is a constant containing the focal length f of the lens and the amplitude l_0 of the incoming light. The symbol J_n stands for the Bessel

function of order n .

With these equations it is possible to calculate all properties that are important for microscopy. The electrical, the magnetically and the total energy distribution have the form

$$\left. \begin{aligned} \langle w_e(u, v, \phi_P) \rangle &= \frac{A^2}{16\pi} \left\{ |I_0|^2 + 4|I_1|^2 \cos^2 \phi_P + |I_2|^2 + 2 \cos 2\phi_P \Re(I_0 I_2^*) \right\} \\ \langle w_m(u, v, \phi_P) \rangle &= \frac{A^2}{16\pi} \left\{ |I_0|^2 + 4|I_1|^2 \sin^2 \phi_P + |I_2|^2 - 2 \cos 2\phi_P \Re(I_0 I_2^*) \right\} \\ \langle w(u, v, \phi_P) \rangle &= \frac{A^2}{8\pi} \left\{ |I_0|^2 + 2|I_1|^2 + |I_2|^2 \right\} \end{aligned} \right\} \quad (1.8)$$

As expected, the total energy density is independent of the angle ϕ_P . Not as obvious from the equations, but given by the symmetry of the arrangement is that the electrical energy distribution turns into the magnetically energy distribution if turned by 90° .

Also interesting is the Poynting²-vector \vec{S} that describes the energy flux density of the electromagnetic field in the propagation direction. Its time average can be calculated with the equations

$$\left. \begin{aligned} \langle S_x \rangle &= \frac{cA^2}{4\pi} \cos \phi_P \Im \{ I_1 (I_2^* - I_0^*) \} \\ \langle S_y \rangle &= \frac{cA^2}{4\pi} \sin \phi_P \Im \{ I_1 (I_2^* - I_0^*) \} \\ \langle S_z \rangle &= \frac{cA^2}{8\pi} \{ |I_0|^2 - |I_2|^2 \} \end{aligned} \right\} \quad (1.9)$$

For the case of the electrical energy density (Equ. (1.8)) we will discuss what happens to the field distribution with increasing aperture angle. In Fig. 1.3 the electrical energy density is shown in the focal plane ($u = 0$) for different aperture angles α as a function of the optical coordinate v . The case $\alpha = 0^\circ$ corresponds to the case of section 1.3.2, the transition to small aperture angles. For $\alpha = 90^\circ$ the light comes from the complete half space. A cut through the center of the profile, as well as a 10-fold magnification is shown above and to the right of each graphic. The initial polarization of the electrical field is horizontal.

²The Poynting-vector was defined by John Henry Poynting.

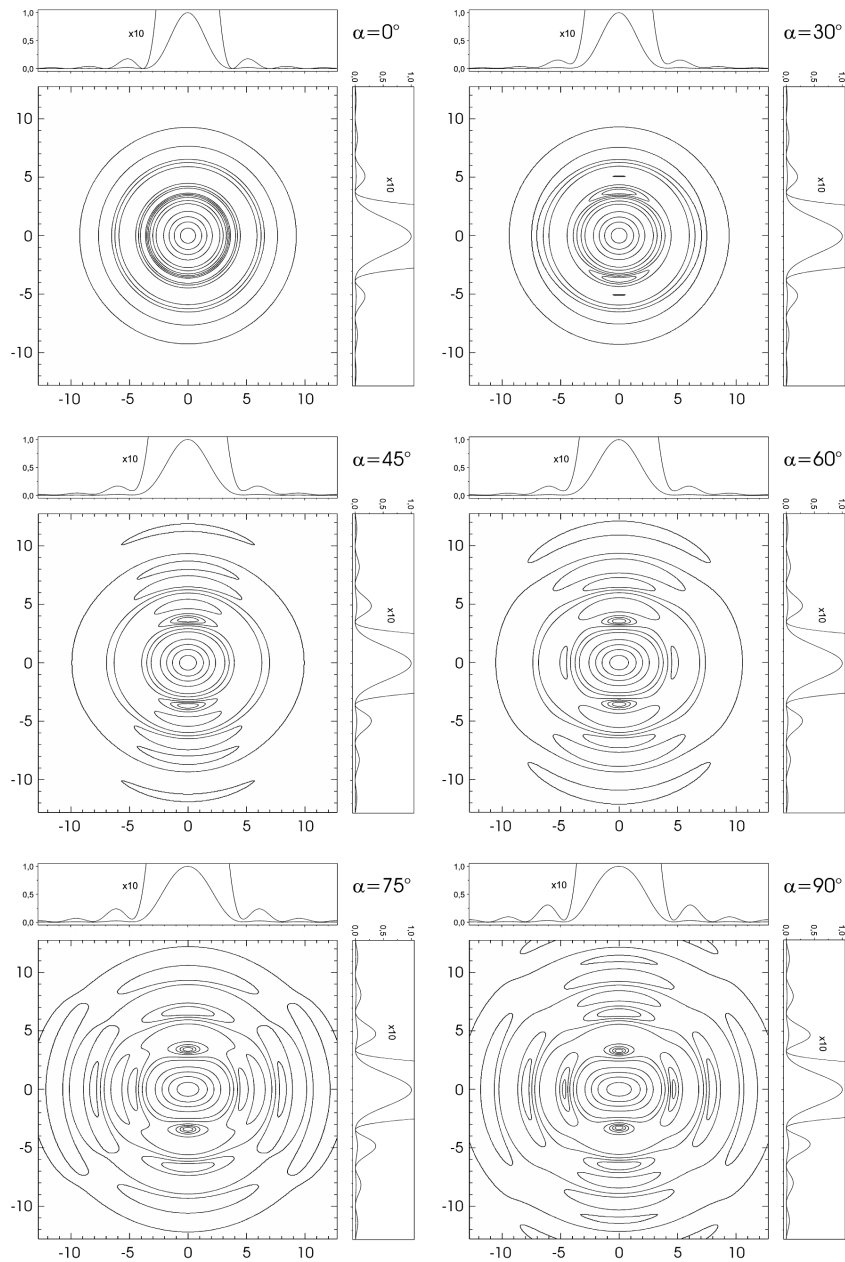


fig. 1.3: Electrical energy density $w_e(u, v, \phi_P)$ in the focal plane ($u = 0$) for different aperture angles α as a function of v . The initial polarization of the electrical field is horizontal ($\phi_P = 0$). The contour lines show the heights 0.002, 0.005, 0.01, 0.02, 0.05, 0.1, 0.3, 0.5, 0.7 and 0.9. A cut through the center of the profile, as well as a 10-fold magnification is shown above and to the right of each graphic.

In Fig. 1.3 one can see, that the electrical energy density drastically changes with increasing aperture angle. The width of the field distribution as a measure for the optical resolution becomes strongly anisotropic. In the cut through the center, parallel to the direction of polarization, one can see even for small aperture angles that the minima do not go back to zero any more. The side maxima are getting larger with increasing aperture angle and reach a relative hight of 4,3 % for $\alpha = 90^\circ$. This is more than twice of the value at $\alpha = 0^\circ$ (1,8 %).

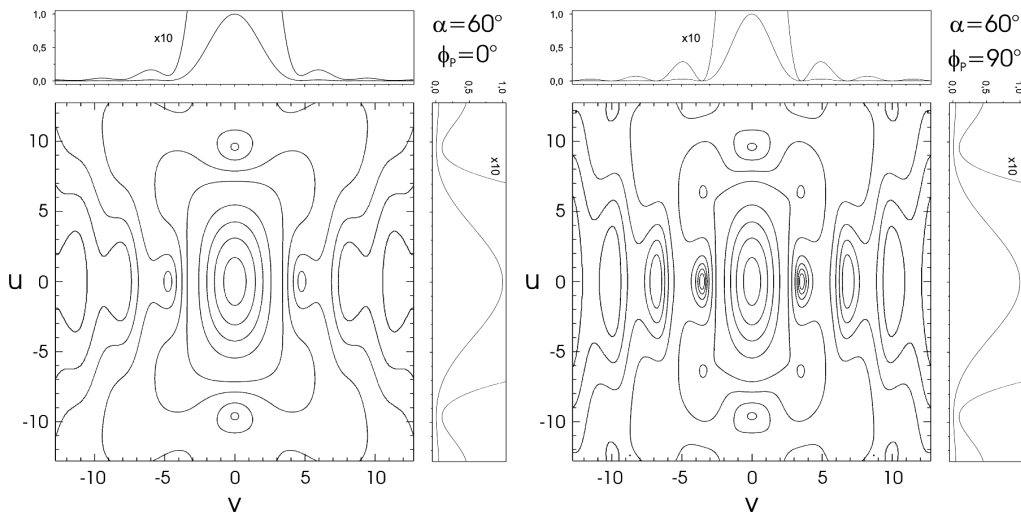


fig. 1.4: Cut through the electrical energy density $w_e(u, v, \phi_P)$ for $\alpha = 60^\circ$. The optical coordinate u is plotted vertical, while the optical coordinate v is plotted horizontal. In the left image, the polarization of the electrical field is horizontal (in the image plane), while in the right image it is pointing out of the image plane. The contour lines show the heights 0.002, 0.005, 0.01, 0.02, 0.05, 0.1, 0.3, 0.5, 0.7 and 0.9.

Fig. 1.4 shows the field distribution in axial direction. The figure shows a cut through the electrical field distribution w_e vertical to the focal plane. The position of the focussing lens would be above (or below) the figure. In the left image, the polarization of the electrical field is horizontal (in the image plane), while in the right image it is pointing out of the image plane.

Again one can see that the electrical energy distribution is highly anisotropic. Even in axial direction the minima do not go back to zero.

1.3.2 Transition to small aperture angles

The theory in the last paragraph is appropriate to describe vector properties of light, but it is too complicated for a simple understanding. If one permits only small aperture angles I_1 and I_2 can be set zero, because for small x the relation $J_n(x) \sim x^n$ is fulfilled. The equations (1.5) and (1.6) simplify to

$$\begin{aligned} e_x &= h_y = -iAI_0 \\ e_y &= e_z = h_x = h_z = 0. \end{aligned}$$

The initial polarization is preserved for small aperture angles. I_0 can be written so that the integral gets independent of α

$$\left. \begin{aligned} I_0(u, v) &= \alpha^2 e^{\frac{i u}{\alpha^2}} h(u, v) \\ h(u, v) &= 2 \int_0^1 \rho J_0(\rho v) e^{\frac{1}{2} i u \rho^2} d\rho \end{aligned} \right\} \quad (1.10)$$

The function $h(u, v)$ is called 3-D Point Spread Function (PSF). It is normalized, so that $h(0, 0) = 1$. The PSF can be interpreted as a Greens function that describes the image of an infinite small point. The approximation of small aperture angles simplifies the theoretical calculation, but is unfortunately connected with a strong restriction. As a comparison, Fig. 1.5 shows the full width at half maximum (FWHM) of the electrical energy density at $u = 0$ as a function of the aperture angle. The dashed line corresponds to the theory for small aperture angles, whereas the solid lines represent the correct theory for a cut parallel and vertical to the polarization direction. The width of the total energy density w (Equ. (1.8)) is shown as a dotted line. The total energy density w is better suitable for a comparison, because w is rotation symmetric, just as the field distribution for small aperture angles.

As expected, all curves are equal for small aperture angles. With increasing α the difference between the curves gets larger and larger. At an aperture angle of only $\alpha = 40^\circ$ the deviation between the curves is larger than 4%.

Oil- and water- immersion objectives can not be adequately described by this theory, because their aperture angle is typically between $55^\circ - 70^\circ$. For this case, the deviation of the FWHM is more than 10%.

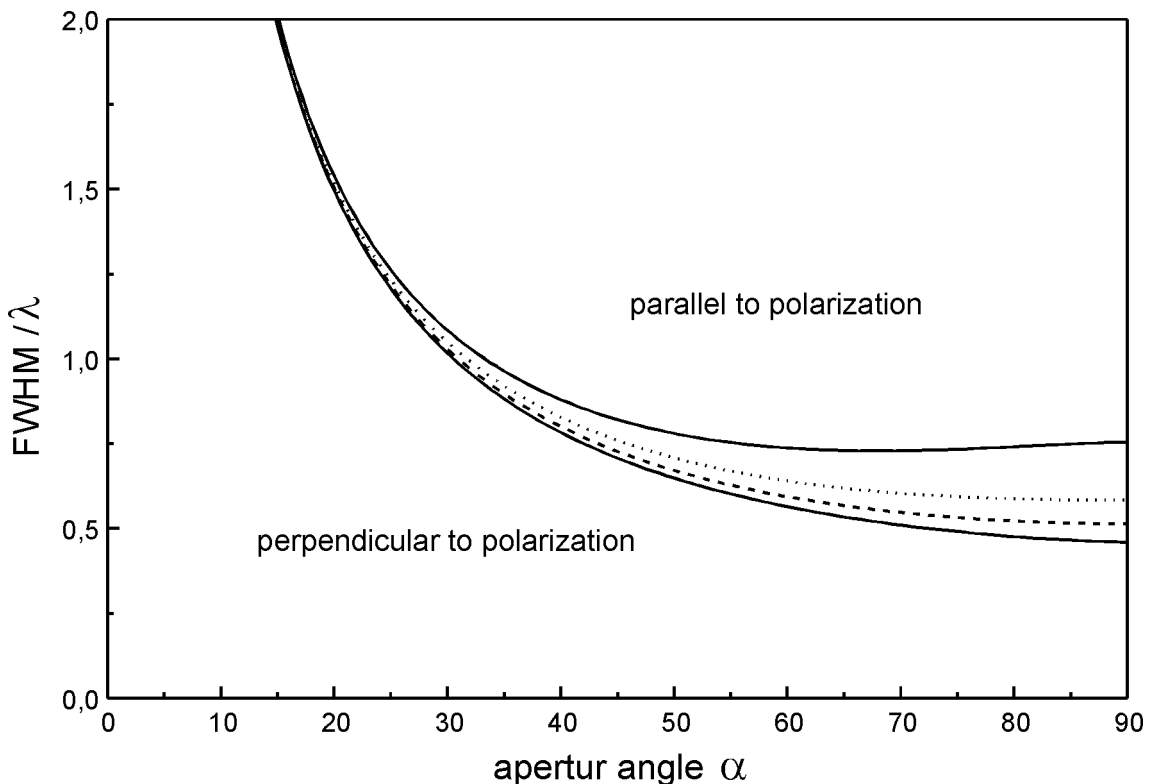


fig. 1.5: Full width at half maximum (FWHM) of the field distribution in the focal plane, solid lines: electrical energy density, dotted line: total energy density, dashed line: electrical or total energy density for small aperture angles.

In Fig. 1.5 one can also see, that an increase of the aperture angle above 70° results only in a very small increase in resolution. A technical realization above this angle is therefore of little use.

1.4 Theory of image formation

One of the most important properties of a confocal system is the point spread function (PSF), which is mainly determined by the microscope objective. This can be the electrical, magnetically or total energy density in the focus. If a sample system couples only to the x-component of the electrical field, the PSF of the excitation would only contain this component. The PSF of the detection can be different. This depends on the emitted light itself, and on the properties of the detector. Of course

it would be better, if one could measure the PSF for every application. In this case, a deconvolution of the image would be possible without additional assumptions. In Ref. [5] a simple interferometric measurement setup is described that makes the measurement of the PSF possible. As a result, one not only gets the amplitude of the function $h(u, v)$, but also the phase. Especially the phase is very important for a coherent image formation.

In the following paragraphs, h_1 stands for the PSF of the excitation and h_2 for the PSF of the detection. For simplification, both functions should be only scalar values. The modification of the light due to the sample can also be described by the scalar function $\tau(x, y, z)$. In general, τ is a complex function that influences amplitude and phase of the electromagnetic field.

1.4.1 Microscope

The formation of the image in a microscope with point-like excitation and large detector is far more complicated than the image formation in a confocal system (with point-like detector). The reason is that the image formation is partly coherent. Both extremes can be mathematically described as following

$$I = |h_1|^2 \otimes |\tau|^2 \quad \text{incoherent image formation} \quad (1.11)$$

$$I = |h_1 \otimes \tau|^2 \quad \text{coherent image formation.} \quad (1.12)$$

The difference between both cases is that for an incoherent image formation the intensities, and for the coherent image formation the amplitudes have to be added. This difference can be illustrated with the following example. Consider the image formation of two points that have the distance of the Rayleigh limit³.

³The Rayleigh criterion says that two points can be optically resolved, if one point sits in the first minimum of the PSF of the second point.

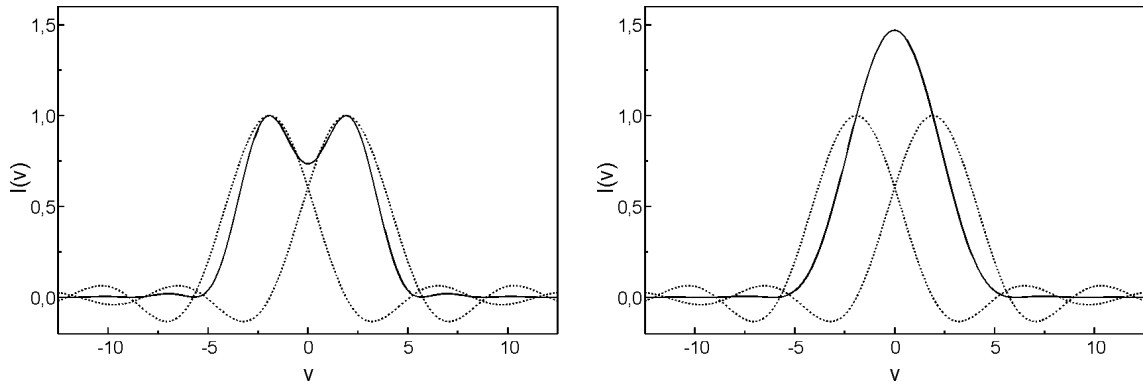


fig. 1.6: Intensity distribution of two points that fulfil the Rayleigh criterion, left: incoherent image formation after Equ. (1.11), right: coherent image formation after Equ. (1.12).

For the incoherent image formation, the two points are easily resolved (minimum). In the case of the coherent image formation, both points can not be separated any more.

The imaging quality of the detection, described by function h_2 is not important here.

1.4.2 Confocal microscope

Due to the point-like excitation and detection, the image formation in a confocal microscope has to be described as coherent. This can be described with the equation

$$I = |(h_1 h_2) \otimes \tau|^2 \quad \text{confocal imaging} \quad (1.13)$$

after (Ref. [6]). The product $h_{eff} = h_1 h_2$ is called effective PSF of the optical system. If one inserts the delta function $\delta(\vec{x})$ for τ , one gets the intensity point spread function. This function is plotted in Fig. 1.7 for a conventional and a confocal microscope. The FWHM differs roughly by a factor of $\sqrt{2}$.

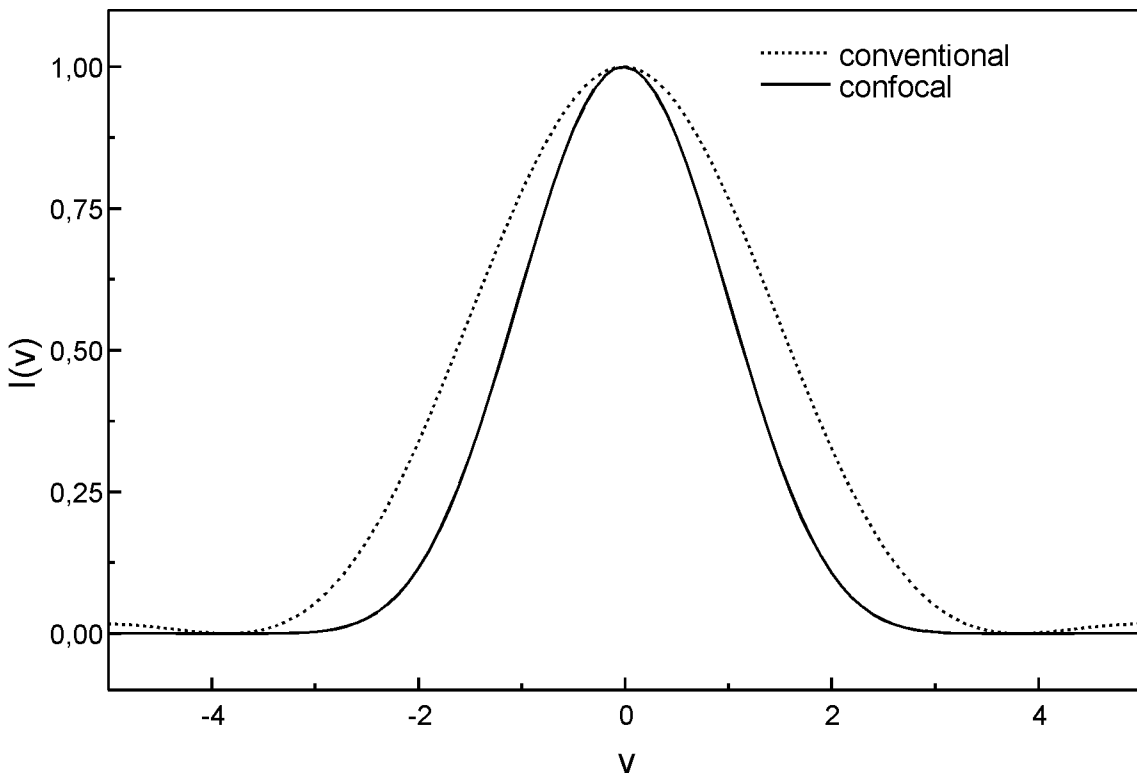


fig. 1.7: Comparison of the intensity PSFs: $I_{conventional} = \left(\frac{2J_1(v)}{v}\right)^2$, $I_{confocal} = \left(\frac{2J_1(v)}{v}\right)^4$.

1.4.3 Confocal fluorescence microscope

The image formation of a confocal fluorescence microscope is strongly different from the case in section 1.4.2. This is due to the statistical nature of the fluorescence. If we consider two non-interacting fluorescent dyes, then none of the dyes knows when the other will fluoresce and there will be no fixed phase relation between them. Therefore we have the case of an incoherent image formation.

The fluorescence is, if not saturated, proportional to the exciting intensity $|h_1|^2$ and the fluorescence generation $f(x, y, z)$. The resulting equation for the intensity distribution of the resulting image in a confocal fluorescence microscope is therefore [7]

$$I = |h_{eff}|^2 \otimes f \quad (1.14)$$

with

$$\begin{aligned} h_{eff} &= h_1(u, v)h_2\left(\frac{u}{\beta}, \frac{v}{\beta}\right) \\ \beta &= \frac{\lambda_2}{\lambda_1} \end{aligned}$$

The optical coordinates u and v are referred to the wavelength λ_1 of the excitation light. This theory is not completely correct, because the wavelength of the fluorescence light has a certain frequency distribution and not only a single wavelength λ_2 . In principle, one has to integrate over all fluorescence wavelengths. If the fluorescence wavelength is evenly distributed around a certain wavelength λ_{max} the error will be small if one replaces λ_2 with λ_{max} . But especially because of the inevitable use of edge filters that absorb the excitation light, the maximum of the fluorescence distribution hitting the detector will be shifted towards the red part of the spectrum. If the filter characteristic is steep, the fluorescence distribution can be very asymmetric and the complete spectrum has to be taken into account.

1.4.4 2-Photon-Microscope

In conventional fluorescence excitation, a dye molecule absorbs a photon of appropriate energy. This is usually only possible, if the energy of the photon is equal or larger than the energy difference of two energy levels in the molecule. If one uses a photon with an energy half of this energy difference, usually no fluorescence excitation is possible.

With the Heisenberg uncertainty relation

$$\Delta t \cdot \Delta E \geq \frac{\hbar}{2}$$

one can calculate, how long the molecule stays in the so called virtual state between both energy states. If a second photon hits the molecule when it is in this virtual state, it is possible to further excite the molecule to the upper energy state. Because of the fact that this is usually not observed, one sees that the probability for this kind of excitation must be very small. If one calculates the lifetime of the virtual state, one finds that the second photon must hit the molecule within roughly $4,2 \cdot 10^{-16} s$. Even if one would be able to focus $1 mW$ of laser power onto the molecule (which is an incredible large power density, because of the small absorption cross section of the molecule), within this time only 1-2 photons would

pass by. The probability for the excitation of the dye is therefore extremely low. Increasing the excitation power is normally not possible, because only few sample systems can withstand high excitation doses without damage. The energy density in the focus of a 1 mW laser beam is about $10^9 \frac{W}{m^2}$, which is more than 30000-times the energy density on a cooking plate. The smallest absorption of the sample would immediately lead to thermal destruction of the sample.

The secret of 2-photon excitation is to use short light pulses of high power. Then the probability of a 2-photon excitation is greatly enhanced, while the thermal load on the sample is kept low. As long as the dye molecules are not saturated, the fluorescence is proportional to the square of the intensity $|h_1|^4$ and to the fluorescence generation $f(x, y, z)$ [8]. The image formation can be mathematically described by

$$I = |h_1\left(\frac{u}{2}, \frac{v}{2}\right)|^4 \otimes f \quad (1.15)$$

The optical coordinates are referred to half of the excitation wavelength. Because the image formation is not confocal, this equation is independent of the PSF of the detection. Even without using a pinhole one still gets a three dimensional image of the sample, because the light intensity is a quadratic function in the image equation and an effective 2-photon excitation is only possible in a small focus area.

1.4.5 Confocal 2-Photon-Microscope

Again, an increased resolution is possible, if the 2-photon fluorescence light is focussed through a pinhole in front of the detector [9, 10]:

$$I = |h_1\left(\frac{u}{2}, \frac{v}{2}\right)|^4 |h_2\left(\frac{u}{\beta}, \frac{v}{\beta}\right)|^2 \otimes f. \quad (1.16)$$

In this case the same problems as discussed in the section about conventional confocal microscopy occur. Because of the confocal image formation, the resolution compared to 2-photon microscopy without pinhole can be increased by a factor of nearly 2. If one uses the same objective for excitation and detection, the chromatic abberation of the objective can cause problems, because it might not be designed for such a large wavelength range. If one uses a system with two objectives, the chromatic abberation can be compensated for by shifting the pinhole to the correct position.

1.5 Image formation for light scattering

In the following two sections, the resolution of a confocal microscope as a function of pinhole size will be discussed. Since the achievable resolution strongly depends on the sample properties, these statements can not be taken as valid in general but are true only under optimum conditions. For all calculations, the point spread function $h(u, v)$ (Equ. (1.10)) was used.

1.5.1 Scattering point

In the following, we consider the scenario of Fig. 1.8, where a scattering point is scanned laterally across the excitation focus.

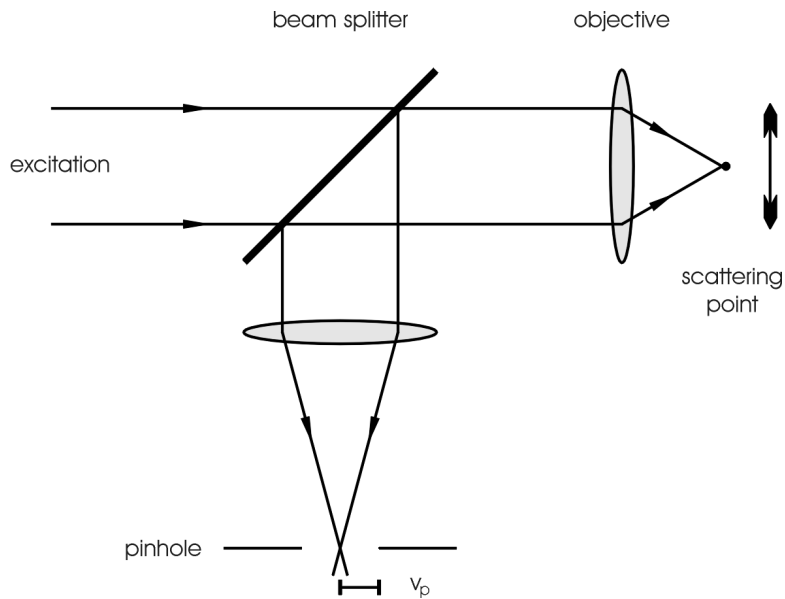


fig. 1.8: Confocal setup for a scattering point.

Up to now, all calculations have been done for an infinitesimal small point detector. Now we replace this point detector with a real two-dimensional detector of radius v_p . This is the reason, why the PSF h_2 in Equ. (1.17) has to be convolved with the detector function D , to obtain the effective PSF for the detection. Since we consider only a single scattering point in the object space, the convolution

with the object itself is not necessary. After Ref. [11] we get the intensity distribution

$$I = |h_1|^2(|h_2|^2 \otimes D) \quad . \quad (1.17)$$

The FWHM of $I(u = 0, v)$ is plotted in Fig. 1.9 as a function of the detector radius v_P . As can be seen, the detector radius should be below $v_P = 0,5$ for highest resolution. If the detector radius is larger than about $v_P = 4$, the resolution will be the same as for conventional microscopy. Even in this case, stray light suppression remains as an advantage over conventional microscopy.

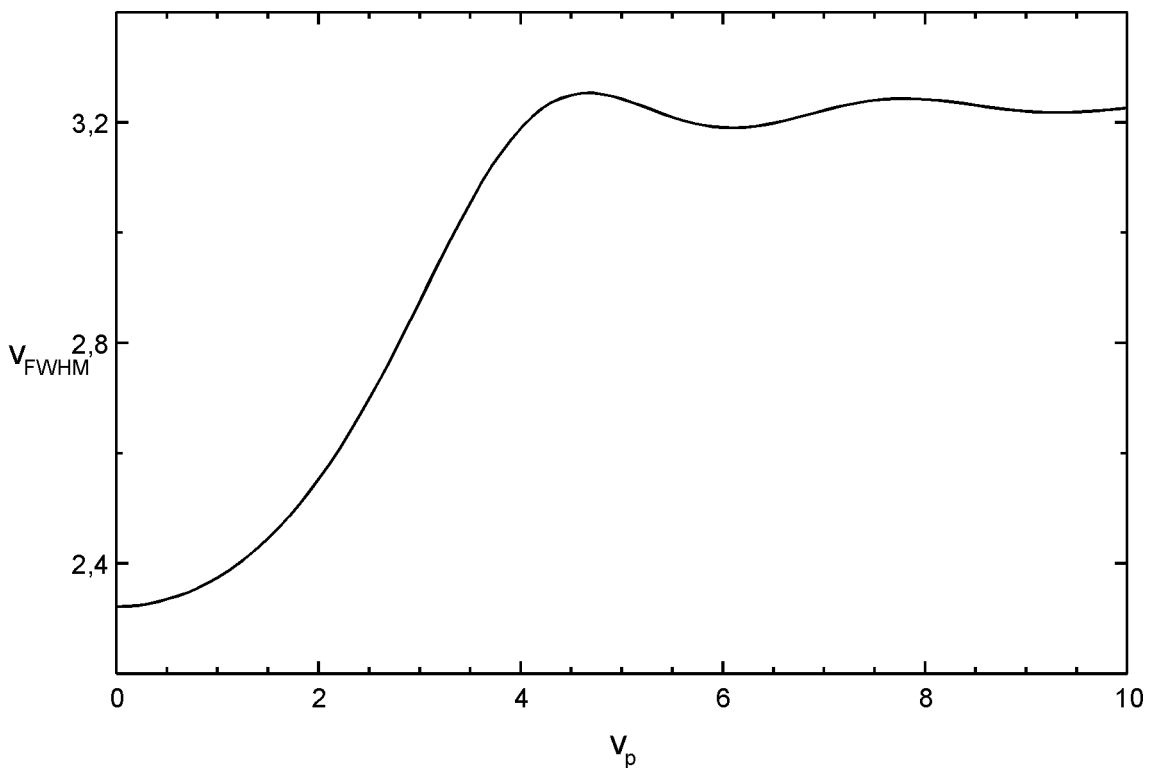


fig. 1.9: Lateral resolution of a scattering point as a function of detector size v_P .

1.5.2 Reflection at a mirror

The quality of the image can be easily checked, by acquiring the signal while a mirror is scanned axially through the focus (Fig. 1.10).

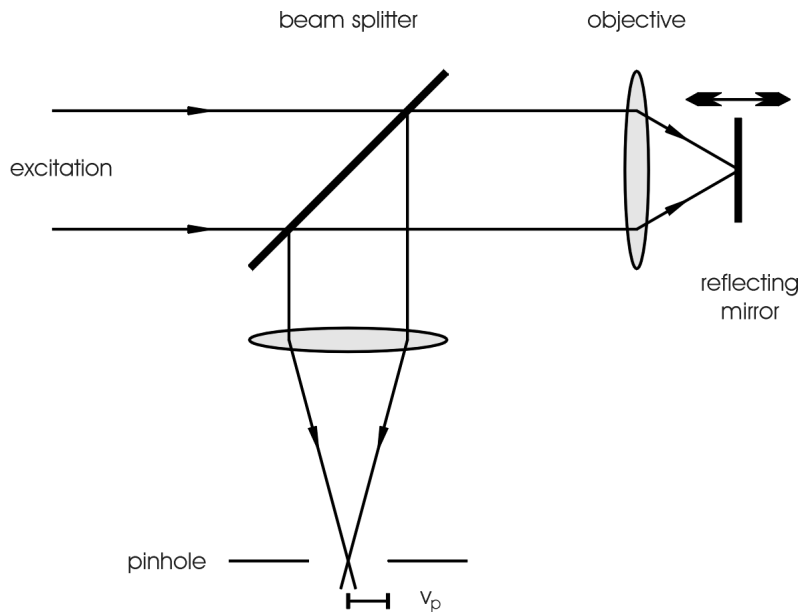


fig. 1.10: Confocal setup for the reflection at a mirror surface.

Since the whole mirror plane reflects the light, the following integral [11] has to be calculated

$$I_{plane}(u) = \int_0^{v_p} |h(2u, v)|^2 v dv . \quad (1.18)$$

From Fig. 1.11 one can see that there is no loss in depth resolution up to a detector radius of $v_P = 2,5$. If the detector radius gets larger than $v_P = 3,5$ the depth resolution decreases linearly with increasing detector radius.

The depth resolution of a reflecting point shows a different behavior. For small detector radii, the resolution is worse than for a reflecting layer, but for larger radii the width gets nearly constant. At $v_p = 10$, the depth resolution is not better than for a conventional microscope with point-like excitation, but if a homogeneous layer is investigated, no axial resolution is possible with a conventional microscope.

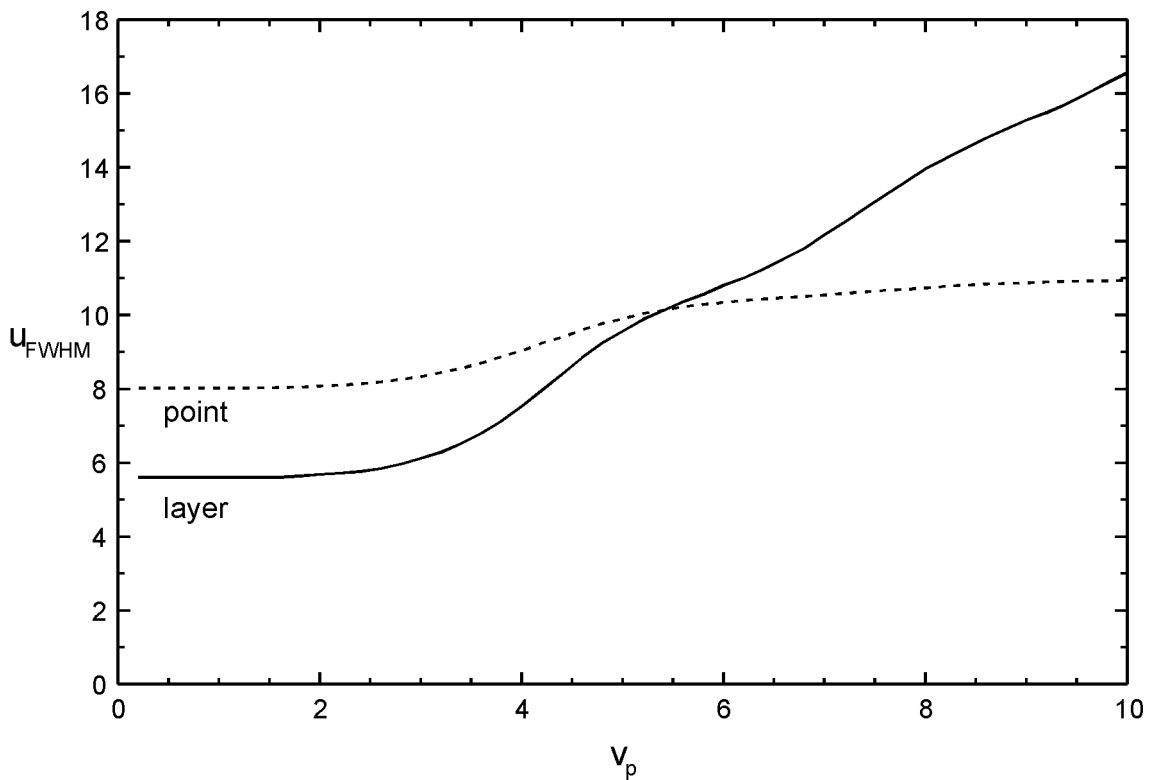


fig. 1.11: Comparison of the depth resolution for a point and a reflecting layer as a function of detector size v_p .

Since no lens aberrations are taken into account, Equ. (1.18) is symmetric to $u = 0$. In reality, the distribution usually looks different. There will be drastic changes or if the setup is not optimized for the objective, or the cover glass correction is not considered. A wrong pinhole position is also immediately visible. Examples for this will be shown in section 3.1.

1.6 Image formation for fluorescence

As discussed in section 1.4.3 the image formation for fluorescence is strongly different to the case of a scattering object. As an example, the resolution for a fluorescing point and a fluorescing layer will be calculated analogue to the last section.

1.6.1 Fluorescing point

Equ. (1.14) is the basis for the curves, shown in Fig. 1.12. v_P is the detector radius.

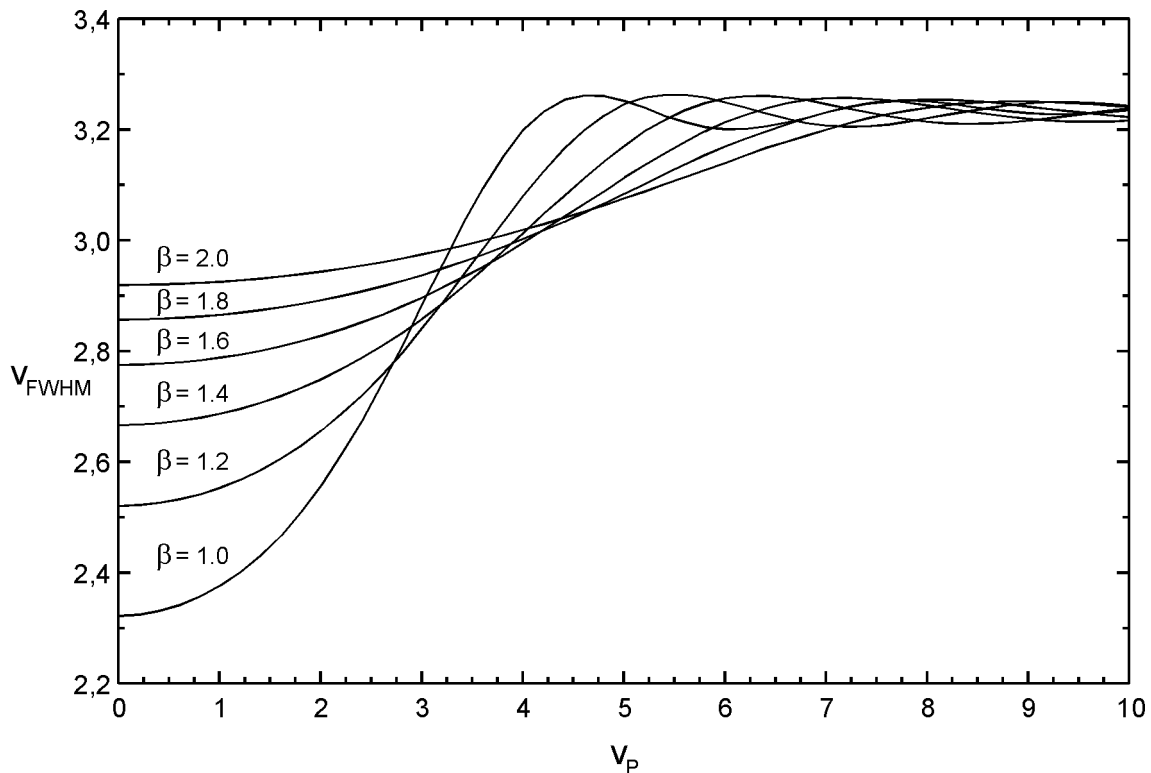


fig. 1.12: Lateral resolution for a fluorescing point as a function of detector size v_P for different β .

The fluorescence emission wavelength is usually shifted by a certain factor relative to the excitation wavelength. This is considered for by the parameter β , which is the ratio between fluorescence and excitation wavelength. For $\beta = 1$ the resolution is the same as for a scattering point. With increasing shift of the fluorescence wavelength, the resolution decreases. If a small loss in resolution is accepted, one sees that the pinhole size should not be adjusted to the excitation, but to the fluorescence wavelength. If the wavelength shift is large, one should use a larger pinhole in order to avoid an unnecessary loss in signal.

For large pinhole sizes, all curves converge. Here again the case of a conventional microscope with point-like excitation is reached. In this case, the resolution is determined only by the excitation wavelength.

1.6.2 Fluorescing layer

The axial resolution at a fluorescing layer differs strongly from the resolution at a reflecting surface. The reason is mainly not due to the wavelength shift but rather due to the incoherent image formation.

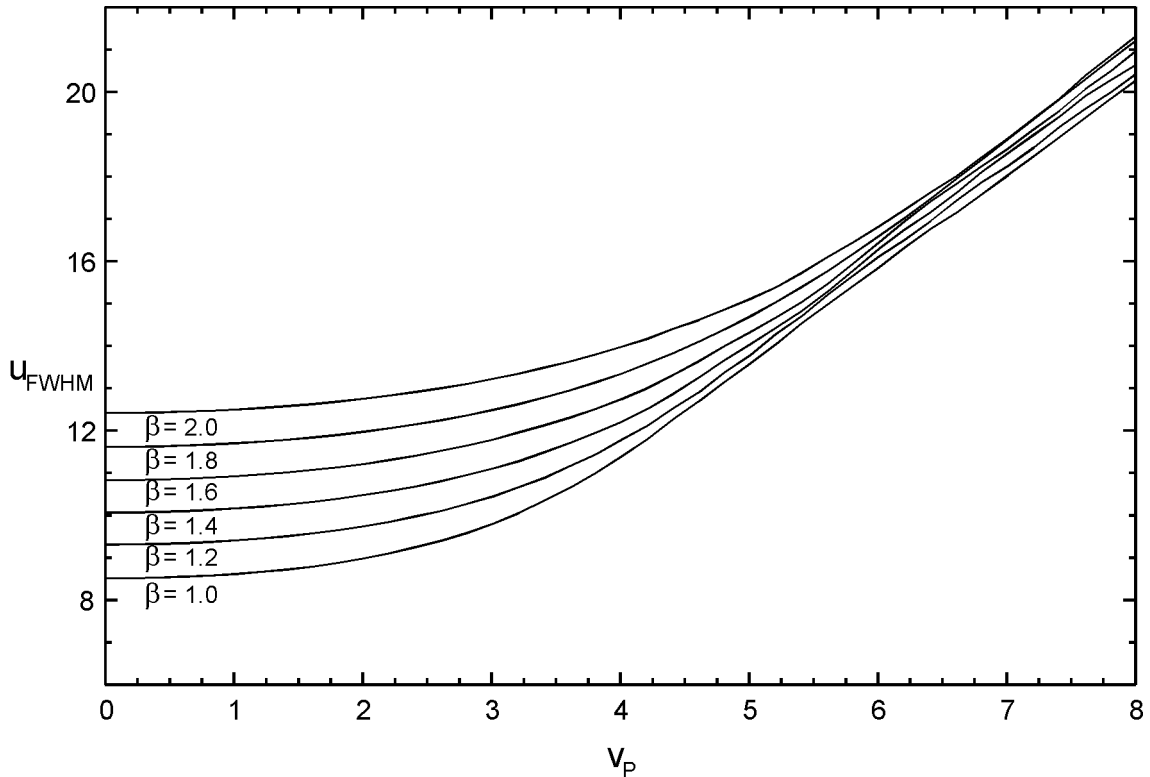


fig. 1.13: Depth resolution at a fluorescing layer for different β as a function of detector size v_P .

To calculate the axial point spread function $I_{CF}(u)$ of a fluorescing layer in a confocal microscope, one has to integrate over the intensity point spread function $I(u, v, \beta)$ (after [8]):

$$I_{CF}(u) = \int_0^{\infty} I(u, v, \beta) v dv$$

The best depth resolution achievable at a reflecting surface was $u = 5, 6$, whereas the best depth resolution for a fluorescing layer without wavelength shift is only $u = 8, 5$ (Fig. 1.11 and Fig. 1.13). This is getting even worse with increasing wavelength shift β . Again, the detector size can be up to $v_P = 2, 5$ without a loss in resolution.

1.7 Near-field microscopy

In confocal microscopy, a slightly higher resolution compared to conventional microscopy is achieved by focussing a point-light source (laser) onto the sample and subsequent collection of the reflection/fluorescence through a pinhole. The lateral restriction of the excitation ensures that the information for the image formation comes only from a small part of the sample. Because of the point-like detection, the volume that contributes to the image formation process is further reduced.

Since the excited, as well as the detected volume depends on the wavelength, the gain in resolution in confocal microscopy is restricted. If one compares the laser-scanning microscopy with a view through the ocular, then in the first case the resolution is given by the excitation wavelength while in the second case the resolution is given by the fluorescence wavelength. Therefore, a loss in resolution of about 10 – 20% due to the wavelength shift between excitation and detection arises. It is obvious, especially for fluorescence microscopy that a substantial increase in resolution can only be achieved, if the excitation focus is as small as possible. The confocal detection ensures three-dimensional image information and a low background, but because of the larger fluorescence wavelength the gain in resolution through confocal detection is not very significant (see Fig. 1.12).

If the image formation is already diffraction limited, the resolution can only be increased, if the wavelength of the excitation light is reduced. But there are strong limitations for the technical realization of this, because for wavelengths below 380 nm most optical glasses used in the design of objectives begin to fluoresce themselves or are getting opaque. In addition, many samples are easily destroyed by UV-light.

Several advanced confocal techniques like 4Pi- or Theta-microscopy [13][14] have been developed in the last years to push the resolution of the optical microscope a little bit further, but they are only of academic interest. These techniques are very complicated (interferometric stable setup) and restricted to special sample systems (thin samples, point samples) and no commercial system using these techniques is available up to now.

The only possibility to overcome the diffraction limit, inherent in all conventional or confocal setups, is to use the so called scanning near-field optical microscopy

(SNOM or NSOM).

Already back in 1928, Synge [15] suggested to avoid the diffraction limit by scanning a tiny aperture in close proximity across the sample. If this aperture is much smaller than the wavelength of light and the distance to the sample is close enough, the resolution obtainable is only limited by the diameter of the aperture and not by the wavelength any more. A realization of this setup (scanning of a nanometer sized aperture with nanometer precision) was not possible at that time. Therefore it took until 1972, when Ash and Nicholls could show that this concept really works in the microwave regime [16]. With their setup they achieved a resolution of $0,5\text{ mm}$ at a wavelength of 3 cm , which is a resolution of $\frac{\lambda}{60}$.

In 1984 Pohl and coworkers [17] demonstrated for the first time a resolution below the diffraction limit in the optical wavelength range. For their experiments they used etched and coated quartz tips. A big step towards routine applications was done by Betzig et al. [18, 19], who used pulled and metal coated optical single mode fibers.

Although many good results were obtained with these tips, they have several severe disadvantages. First, production is a single piece process. Every tip has to be pulled separately, which makes production very time consuming. Second, due to the long taper, transmission of these tips is very low (typically 10^{-6} for a 100 nm aperture). Third, these fibers are very stiff in vertical direction. Therefore distance feedback is very critical and these fibers easily break during approach or scanning.

Another big step towards user friendliness is due to the introduction of the new cantilever SNOM sensors [20] that are used in the *AlphaSNOM*. These sensors have the size and shape of standard AFM cantilevers and are fabricated in a batch process. The cantilever consist of silicon with a hollow silicon dioxide pyramid at the end (Fig. 2.7). This pyramid has a tiny hole of below 100 nm at its tip and the whole system is aluminium coated. The SNOM excitation is focussed from the backside into the pyramid (Fig. 2.8). A small fraction of the light can pass the aperture and excites the sample in the near-field. A second laser is focussed onto the cantilever and the reflected light is used for standard beam-deflection feedback (like in most AFMs)(Fig. 2.9).

These tips are much more reliable than pulled optical fibers and have a higher throughput. The cantilever can bend in vertical direction and distance feedback

is easy and uncritical. Nearly all AFM distance feedback modes can also be used with this cantilevers. Due to the batch fabrication process, the properties of the cantilevers and apertures are excellent and very homogeneous.

An overview over the near-field microscopy can be found e.g. in the book of M. A. Paesler and P. J. Moyer [21].

1.7.1 Dipole radiation

To compare the properties of the electromagnetic far-field and near-field, an oscillating electrical dipole is considered as a model system (e.g. as an approximation for a fluorescing molecule).

The electric field $\vec{E}(\vec{r})$ and the magnetic induction $\vec{B}(\vec{r})$ of an oscillating dipole are described by [22]

$$\begin{aligned}\vec{B}(\vec{r}) &= k^2(\vec{n} \times \vec{p}) \frac{e^{ikr}}{r} \left(1 - \frac{1}{ikr}\right) \\ \vec{E}(\vec{r}) &= k^2(\vec{n} \times \vec{p}) \times \vec{n} \frac{e^{ikr}}{r} + [3\vec{n}(\vec{n}\vec{p}) - \vec{p}] \left(\frac{1}{r^3} - \frac{ik}{r^2}\right) e^{ikr}\end{aligned}$$

From these equations one can see, that the magnetic induction $\vec{B}(\vec{r})$ is always perpendicular to the radius vector \vec{r} , while the electric field $\vec{E}(\vec{r})$ has components parallel and perpendicular to \vec{r} .

In the far-field (distance from the dipole \gg than the wavelength λ), terms with a $\frac{1}{r}$ distance dependence dominate:

$$\begin{aligned}\vec{B}_{far}(\vec{r}) &= k^2(\vec{n} \times \vec{p}) \frac{e^{ikr}}{r} \\ \vec{E}_{far}(\vec{r}) &= \vec{B} \times \vec{n}\end{aligned}$$

The near-field (distance from the dipole \ll than the wavelength λ) is dominated by terms that decay faster than $\frac{1}{r}$:

$$\begin{aligned}\vec{B}_{near}(\vec{r}) &= ik(\vec{n} \times \vec{p}) \frac{1}{r^2} \\ \vec{E}_{near}(\vec{r}) &= [3\vec{n}(\vec{n}\vec{p}) - \vec{p}] \frac{1}{r^3}\end{aligned}$$

It should be noted that the magnetic induction in the area $kr \ll 1$ is a factor kr smaller than the electrical field. Therefore, the near-field zone is dominated by electrical fields.

Only the far-field components (components prop. $\frac{1}{r}$) are radiated and contribute to the image formation of a conventional (far-field) microscope. These components contain information about spacial frequencies smaller than NA/λ , so that only structures larger than λ/NA can be detected in the far-field.

The near-field components contain the information about higher spacial frequencies but they decay exponentially with distance from the dipole (evanescent waves), which means that they are not radiated and therefore can not be detected in the far-field. This can be understood by the following consideration: If one calculates the part of the electrical energy that is radiated from the dipole, one has to solve the following integral

$$\oint_{\text{surface}} \vec{E}^2(\vec{r}) R^2 d\vartheta d\varphi$$

where the near-field components vanish at larger distances, because

$$\oint_{\text{surface}} \frac{\text{const}}{r^6} R^2 d\vartheta d\varphi = 0 \text{ for } \lim_{r \rightarrow \infty}$$

These electric fields can only be detected if the detection (or excitation) is done in the near-field, very close to the sample. As a rule of thumb, the distance between the illuminating near-field aperture and the sample in aperture-SNOM should be less than the radius of the aperture (< 50 nm for a 100 nm aperture).

Chapter 2

The Instrument

All measurements shown were obtained with the WITec AlphaSNOM. The setup of this instrument combines the advantages of confocal and near-field optical microscopy in a single instrument. A comparison of both techniques at the same sample position is possible as well. Effects introduced due to the interaction of the field gradient at the near-field aperture with the topography can be investigated with a subsequent far-field investigation. One of the advantages of this instrument compared e.g. to biological confocal microscopes is that most of the optical setup is easily accessible. Despite the fact that all measurements in the following sections were obtained with the WITec AlphaSNOM, the results can be transferred to any confocal setup.

2.1 The microscope

The AlphaSNOM used for the experiments in the following chapter has a standard microscope body with Köhler illumination beam path for white light illumination and a microscope turret for 5 objectives. The laser is coupled into the microscope via a single-mode optical fiber. The laser is collimated with an adjustable optics to a parallel beam inside the microscope. A beam splitter directs the parallel beam to the microscope objective, where it is focussed onto the sample. In the basic configuration, every laser between 400 and 700nm can be used as an excitation source. For UV applications below 390nm wavelength, several optical parts inside the mi-

croscope have to be changed. The reason is, that most achromatic lenses use glass types that have strong absorption below 390nm.

For confocal microscopy, the reflected (fluorescent) light is collected with the same objective, passes the beam splitter and is focussed into a multi-mode fiber. The core of the multi-mode fiber acts as the confocal pinhole. The other end of the fiber is connected to the detector. A second microscope is located in a closed box below that also works as a stable base for the upper microscope. Both microscope objectives can be moved independently on the same optical axis. During a measurement, the sample is scanned across the focus with a three axis piezoelectrical scan table. A picture of the microscope and the beam path inside can be seen in Fig. 2.1 and Fig. 2.2 respectively.



fig. 2.1: The instrument

Due to the modular setup of the system, many different measurement configurations are possible. Depending on the pinhole size (core diameter of the multimode fiber) the microscope can be used as a conventional or a confocal microscope, in reflection or transmission, for fluorescence etc. Through the choice of the excitation wavelength, conventional or even 2-photon fluorescence excitation is possible. Due to the detection via multi-mode fiber, coupling of a spectrometer is easily possible. Using the near-field objective, near-field optical experiments are possible with a simple turn of the turret.

2.2 Descriptions of the components

An schematic overview about the different components and the beam path can be found in Fig. 2.2.

2.2.1 Data acquisition

Data acquisition and scanning is performed through a special PCI plug in card in the PC. This data acquisition system has two analogue output channels that are used to control the position of the scan table and 8 differential analogue input channels for simultaneous data acquisition. The scan is controlled by a Windows based program(ScanCtrl). The data acquisition has 16 bit resolution and a sampling rate of 250 kHz. The input range can be configured to either 0 V to +10 V or -10 V to +10 V. Several digital I/O ports are used to create trigger signals synchronous to the scan (pixel trigger, line trigger and image trigger) or synchronize the scan with external devices.

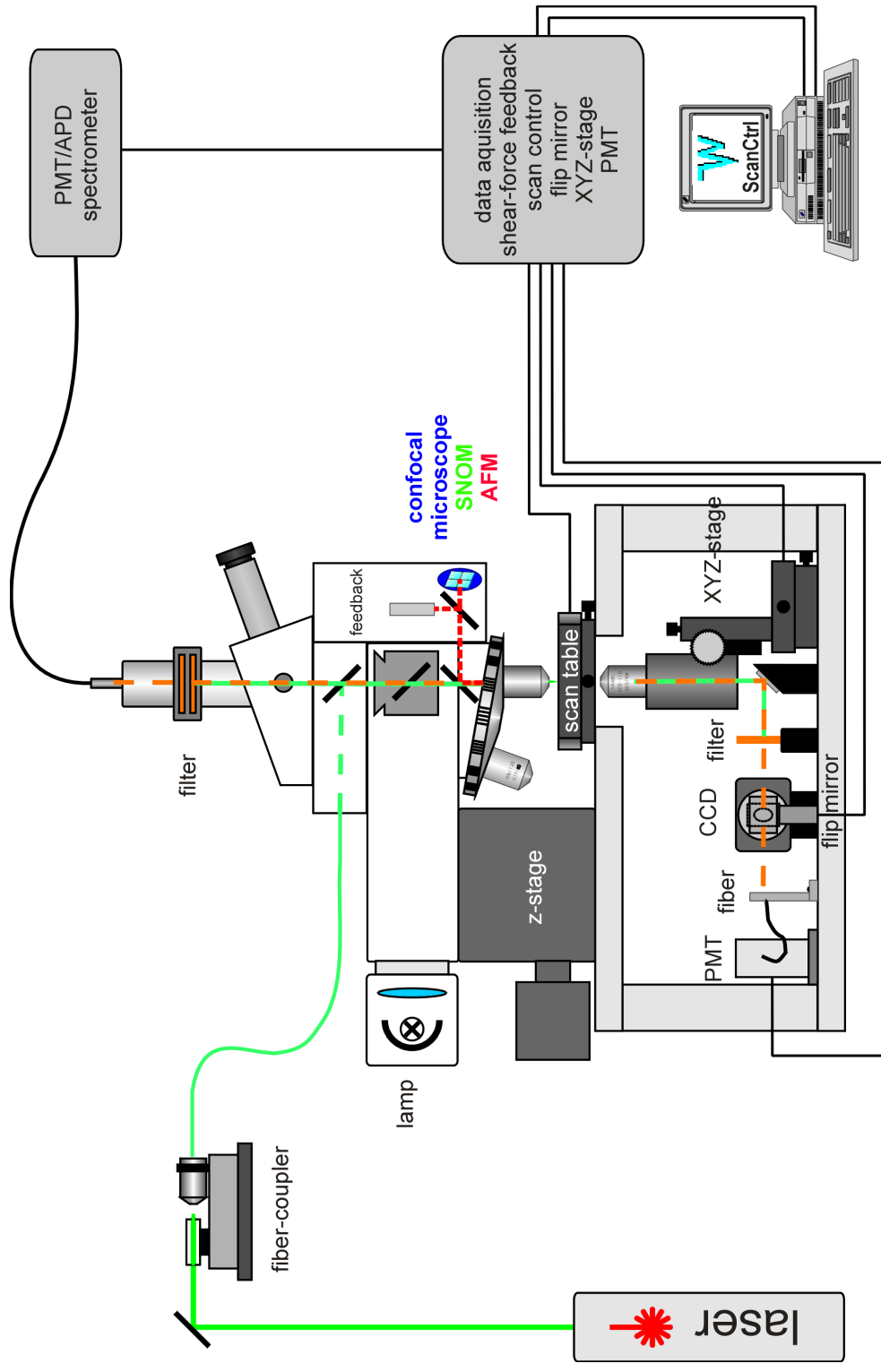


fig. 2.2: Scheme and beam path of the instrument.

2.2.2 Scan table

One of the important properties of a confocal setup is the possibility to acquire three dimensional images. For this, the sample has to be scanned in three dimensions. In the WITec AlphaSNOM and the confocal Raman microscope CRM200, this is done with a piezoelectric scan table. The lateral scan range is $100\text{ }\mu\text{m} \times 100\text{ }\mu\text{m}$ or $200\text{ }\mu\text{m} \times 200\text{ }\mu\text{m}$, depending on the version, the axial scan range is $20\text{ }\mu\text{m}$ for all scan tables. The table has capacitive position sensors that measure the position of the table and therefore compensate for any hysteresis or creep, inherent in all piezo systems. The positioning accuracy of the scan table is $1,5\text{nm}$ (3nm for the $200\text{ }\mu\text{m}$ version) in XY direction and $0,3\text{nm}$ in Z direction.

In many commercial laser-scanning-microscopes, the laser focus is scanned across the sample with a galvanometer scanner. The scan speed of these systems is much higher than what is possible with sample scanning (up to several images per second). But most fluorescence experiments are not limited by the scan speed, but by the number of photons that can be collected per time unit. In practice, many fluorescence experiments have to be performed with slow scanning anyway, so that the table is usually not the limiting factor. Another advantage of a fixed focus is, that all microscope objectives are only used on-axis, where they have their best performance and relatively simple objectives can be used without loss of performance (e.g. no expensive PLAN-objectives are needed).

Besides unrivalled precision of the scan table with capacitive feedback sensors, another advantage of this system is that many scanning probe techniques can be combined in the same instrument. By simply turning the turret, the user can switch between confocal microscopy, near-field microscopy and AFM using the same scan table and therefore the same reference system.

2.2.3 Detector

A photomultiplier¹ (PMT) in photon counting mode was used as detector. This PMT only needs a single $+5\text{ V}$ power supply, has an internal high voltage supply, an amplifier with discriminator and delivers a TTL-pulse for every counted photon.

¹Hamamatsu H6240-01

$\lambda [nm]$	number of photons [$\frac{cps}{pW}$]	quantum efficiency
200	$1,0 \cdot 10^6$	0,13
300	$1,5 \cdot 10^6$	0,16
400	$2,0 \cdot 10^6$	0,17
500	$2,5 \cdot 10^6$	0,14
600	$3,0 \cdot 10^6$	0,12
700	$3,5 \cdot 10^6$	0,021
800	$4,0 \cdot 10^6$	0,0037

Tab. 2.1: Quantum efficiency as a function of wavelength (extracted from the data sheet of the manufacturer).

Because of the relatively good quantum efficiency (Tab. 2.1) between 300 nm and 500 nm and the bad quantum efficiency above 700 nm the photomultiplier (PMT) is suitable for experiments in the blue to green wavelength range as well as for 2-photon excitation with wavelengths of about 700 nm to 1000 nm . The dark count rate of the photomultiplier is below 100 cps . For typical scan velocities ($1\frac{\text{line}}{\text{second}}$ with 512 pixels), the influence of the dark count rate is less than $1\frac{\text{Photon}}{\text{Pixel}}$ and can therefore be neglected. A dark count rate up to 500 cps can usually be neglected, because for these values the dark count rate per pixel is much smaller than the photon noise. The photomultiplier works linear up to $2,5\text{ Mcps}^2$, therefore the count rate should not exceed $4500\frac{\text{photons}}{\text{pixel}}$ at a typical setting of $1\frac{\text{line}}{\text{second}}$ with 512 pixels.

If the sensitivity of the PMT is not sufficient, a photon counting avalanche photodiode (APD) can be used, which has a quantum efficiency of up to 80% at 650 nm wavelength.

2.2.4 Setup for 2-photon excitation

In this section, the setup used for 2-photon excitation is explained. For efficient 2-photon excitation, laser pulses of high peak power are needed. For our experiments

²Deviation from linearity below 10%.

we used a mode-locked Ti:Sapphire laser³. This laser is pumped by an Ar-ion laser with a power of about 12 W . The pulses of the Ti:Sapphire laser have a pulse width of 80 fs and a repetition rate of 82 MHz . The wavelength with the used mirror set could be tuned between 720 nm and 850 nm . The average power of the laser was in the order of 2 W , whereas the peak power in a single pulse was about 300 kW . Due to the shortness of the light pulses, the beam is not monochromatic any more. The minimum spectral width can be calculated with the help of the Heisenberg uncertainty relation $\Delta t \cdot \Delta\omega \approx 1$. With the equation

$$\Delta\lambda = \frac{\lambda^2}{2\pi c} \frac{1}{\Delta t}$$

one calculates a minimum spectral width of 4 nm for a 80 fs -pulse at a wavelength of 780 nm , while the real value was measured to be about 8 nm . If such a short pulse passes lenses, a glass fiber or other optical components, it will suffer from dispersion and the pulse width increases.

2.2.5 Pulse compression with prechirp

Laser light can be coupled into a microscope either with a free beam path or by using the glass fiber technique. The WITec AlphaSNOM/CRM 200 microscopes use, single-mode optical fibers for laser delivery. Depending on the wavelength, lasers can be very bulky and may introduce mechanical noise (due to cooling) to the system. The use of a single-mode fiber has two advantages. First, the microscope is separated from the light source and second, a single-mode fiber provides a gaussian beam profile and is therefore an ideal illumination source for confocal microscopy. The fiber works as a spacial filter and a gaussian beam profile can be focussed diffraction limited onto the sample.

³Spectra Physics, Tsunami 3160 C

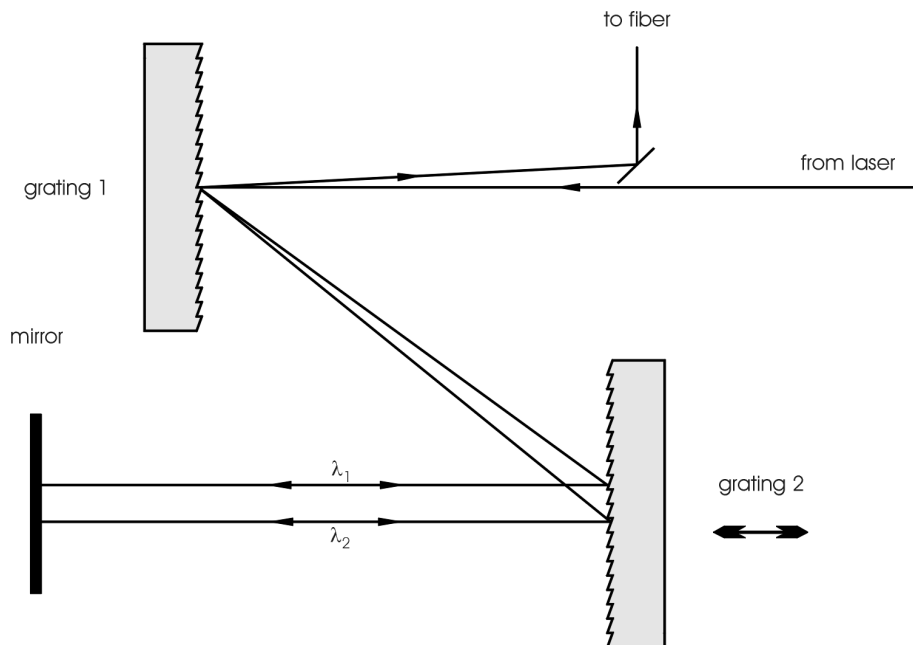


fig. 2.3: Prechirp setup.

A disadvantage of using fibers for 2-photon excitation is that due to their spectral width short light pulses suffer from dispersion and reduce the yield in 2-photon excitation. Due to (normal) dispersion, the "red" part in the spectrum of a short pulse will reach the sample some time before the "blue" part of the spectrum. This pulse broadening can be compensated for by introducing an optical element of anormal dispersion. With a simple setup with two optical gratings and a mirror, as shown in Fig. 2.3, the "red" part of the pulse spectrum is delayed relative to the "blue" part, so that after travelling through the glass fiber they reach the sample at the same time again. With this simple setup however, only the linear dispersion can be compensated. The compensation of higher orders can be done eg. with a setup with prisms.

In the experiment, the grating distance was optimized for the glass fiber and all optical components without objective. The result was checked with an autocorrelator. The result is shown in Fig. 2.4.

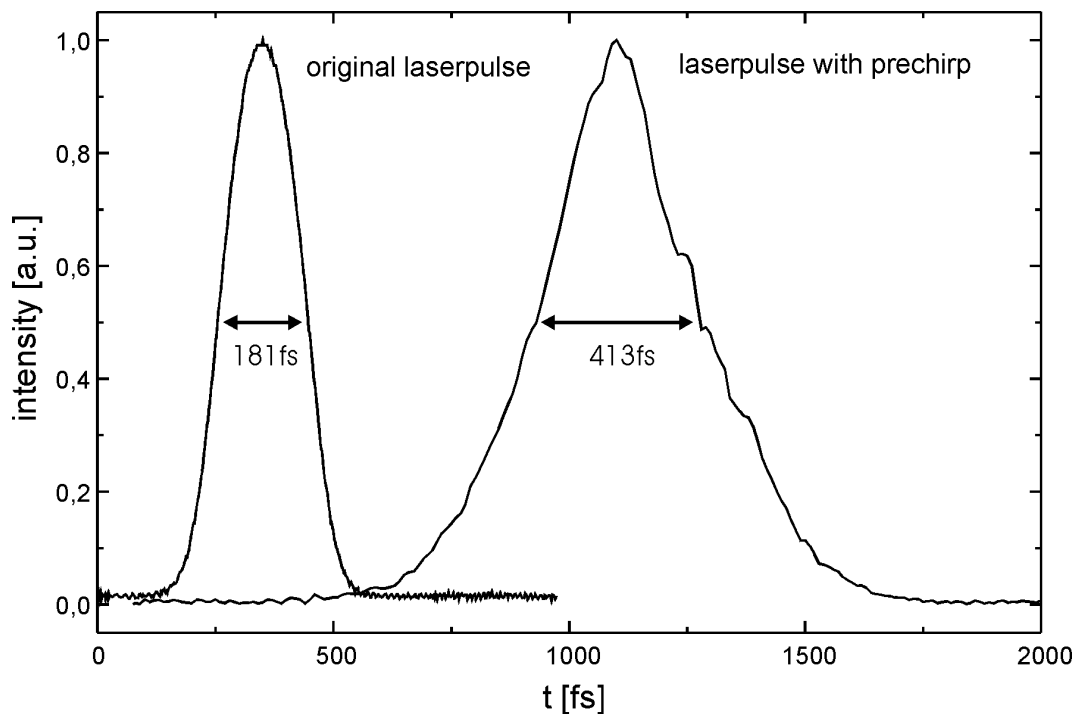


fig. 2.4: Autocorrelation, left: laser pulse directly from the Ti:Sapphire laser, right: laser pulse with prechirp at the sample position (without microscope objective).

If one assumes that the original pulse shape follows a gaussian, the resulting pulse width is 292 fs (deconvolution factor $\frac{1}{\sqrt{2}}$). This is not bad for this simple setup, because without prechirp the pulse width is several picoseconds. For comparison, the light pulse directly from the laser had a pulse width of only 128 fs .

2.2.6 Pinhole size

The binocular of the microscope has a second output port which is equipped with a adjustable fiber coupler for multi-mode fibers. The core of the multi-mode fiber acts as a pinhole for confocal microscopy. The fiber can be adjusted laterally, so that maximum collection efficiency is achieved.

The fiber is protected against mechanical strain and shielded against room light. With the fiber it is simple to direct the light to any detector, e.g. a PMT or a spectrometer.

The lateral position of the pinhole has to be adjusted with micrometer precision

(typical pinhole size $10 - 100 \mu\text{m}$) while the focus position is not very critical. If ΔG is the object size and M the magnification of the objective, then the lateral image size is given by $\Delta B = \Delta G \cdot M$. But what is about the axial magnification? From the image equation for thin lenses one gets the relation

$$\begin{aligned} |\Delta b| &\approx |\Delta g|M^2 \\ \Delta b &\ll b \quad : \text{image distance} \\ \Delta g &\ll g \quad : \text{object distance} \end{aligned} \tag{2.1}$$

Without diffraction limit, an object of axial extension of 200 nm would have a length of 2 mm in the image space at a magnification of $M = 100$. Since the magnification M is quadratic in Equ. (2.1), the depth of focus is very high and the axial position of the pinhole is not critical. The choice of the pinhole size is very important in fluorescence experiments. On one hand the signal should be as high as possible, while on the other hand the image should be confocal.

The size of the pinhole, in optical coordinates, should not exceed $v_{P_{max}} = 2,5$ to avoid a loss in z-resolution. To obtain the highest lateral resolution, the pinhole size should be below $v_{P_{max}} = 0,5$.

In practice, the pinhole size can be up to $v_{P_{max}} = 4$ without significantly changing depth resolution and up to $v_{P_{max}} = 2$ without significantly changing lateral resolution. As shown in section 1.5.1, for $v_{P_{max}} > 4$, only the resolution of a conventional microscope remains.

For the experiment, the relation

$$\frac{M}{N_A} \geq \frac{\pi d_0}{v_{P_{max}} \lambda}$$

must be fulfilled, where M is the magnification, d_0 the diameter of the pinhole and N_A the numerical aperture of the objective. The left side of this equation is defined by the objective and the beam path. In Tab. 2.2, the parameter $\frac{M}{N_A}$ is calculated for several typical objectives.

objective	10/0.25	20/0.4	40/0.6	60/0.8	100/0.9	100/1.25	100/1.4
M/N_A	53	50	67	75	111	80	71

Tab. 2.2: M/N_A for different objectives.

The right side of Equ. (2.2.6) is defined by the wavelength and the pinhole size itself (Tab. 2.3).

wavelength (nm)	440	488	532	633	785
$d_0 = 10\mu m$	29	26	24	20	16
$d_0 = 25\mu m$	71	64	59	50	40
$d_0 = 50\mu m$	142	129	118	99	80
$d_0 = 100\mu m$	286	258	236	199	160
$d_0 = 200\mu m$	571	515	472	397	320

Tab. 2.3: $\frac{\pi d_0}{2.5\lambda}$ for typical wavelengths and pinhole sizes.

With the help of these tables, the correct pinhole size can be determined for any experiment. If an objective with a magnification of $100x$ and a numerical aperture of 0.9 is used at a wavelength of 532 nm , the optimum pinhole size would be $50\mu m$ for maximum depth resolution and $10\mu m$ for maximum lateral resolution.

In real experiments, one usually has to find a compromise between highest resolution and collection efficiency. When a very small pinhole is used, the collection efficiency is strongly reduced. This is plotted in Fig. 2.5.

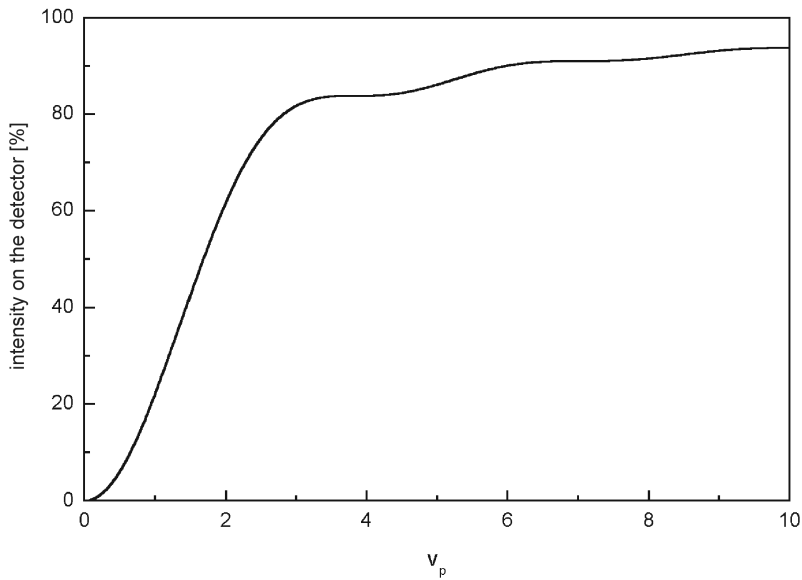


fig. 2.5: Collection efficiency as a function of pinhole size normalized to the total power in the image plane.

This graphic shows the intensity on the detector as a function of pinhole size, normalized to the total intensity in the image plane ($u = 0$ in Equ. (1.18)). One can see that the collection efficiency is about 75% for maximum depth resolution ($v_P = 2, 5$), but only 6% for maximum lateral resolution $v_P = 0, 5$.

For a scattering point (section 1.5.1, $\beta = 1$), the gain in resolution between using a pinhole size of $v_P = 2, 5$ and $v_P = 0, 5$ is only about 16%, while for a fluorescing sample with $\beta = 1, 2$ (section 1.6.2) the gain in resolution is only about 8%, but for both cases the detected intensity is reduced by a factor of 12, 5 .

2.2.7 Near-field setup

For scanning near-field optical microscopy, the *AlphaSNOM* uses its unique Near-Field-Objective (Fig. 2.6). The Near-Field-Objective has the size and shape of a standard microscope objective and is screwed into a free position of the microscope turret. It is used to focus the illumination, as well as the beam deflection laser onto a Cantilever-SNOM sensor.

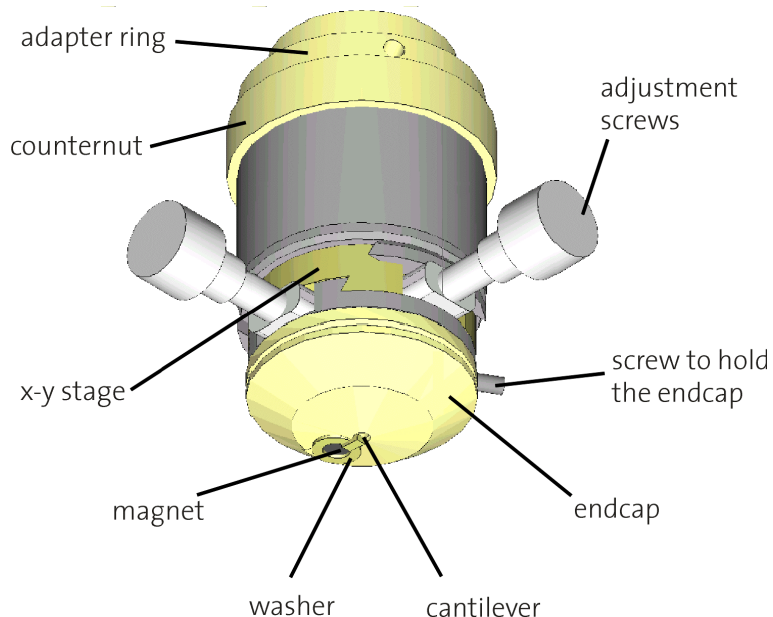


fig. 2.6: Near-Field-Objective.

These Cantilever-SNOM sensors have several advantages over standard pulled optical fibers. They are much more reliable than pulled optical fibers and have a higher throughput. The cantilever can bend in vertical direction and distance feedback is easy and uncritical. Another advantage is that nearly all AFM distance feedback modes can be used with these cantilevers. Due to the batch fabrication process, the properties of the cantilevers and apertures are excellent and very homogeneous. The micro-machined Cantilever-SNOM Sensors are magnetically fixed at the endcap of the Near-Field-Objective. The Near-Field-Objective incorporates also a high precision XY-stage used for moving the Cantilever-SNOM Sensors into the optical axis of the Near-Field-Objective.

The Cantilever-SNOM Sensors consist of a silicon cantilever with a hollow SiO_2 tip. Typical dimensions of the cantilevers are 150 μm width, 700 μm length and 5 μm thickness. The pyramid has a typical base of 10 μm and a height of 8 μm . The cantilevers are Al-coated and have a nanoscopic hole at the center of the pyramid which acts as the near-field aperture. Typical diameter of the near-field aperture for visible wavelength applications is below 100 nm (Fig. 2.7 and Fig. 2.8).

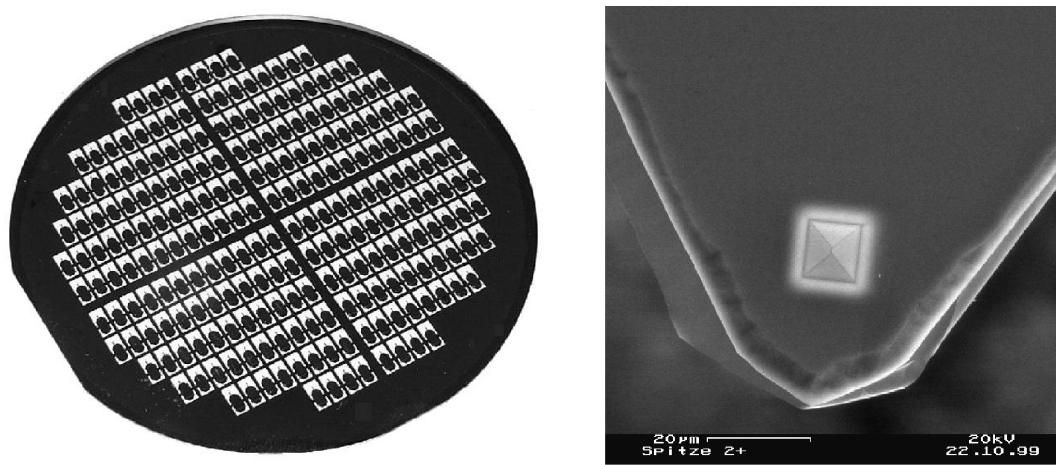


fig. 2.7: Left: Wafer with 228 C-antilever-SNOM sensors. Right: Cantilever with SiO_2 tip.

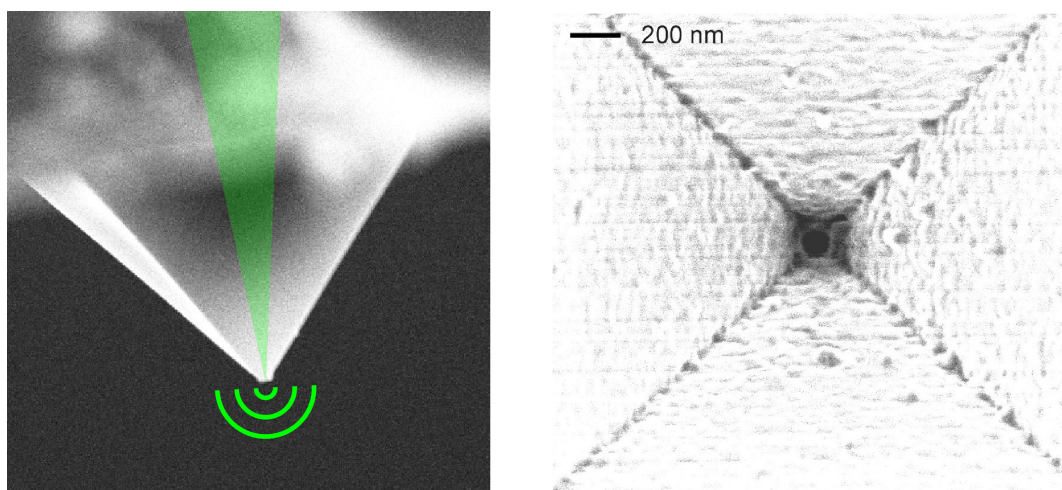


fig. 2.8: Left: The excitation laser (green) is focussed into the backside of the pyramid of the Cantilever-SNOM Sensor. A small portion of the light tunnels through the near-field aperture and is used for near-field optical microscopy. Right: Close-up of a near-field aperture with 100 nm diameter.

The transmitted light intensity is strongly dependent on the ratio of wavelength and aperture. Reducing the aperture diameter by a factor of only two can reduce the transmitted light intensity by several orders of magnitude. The excitation laser (green in Fig. 2.8) is focussed into the backside of the pyramid of the Cantilever-SNOM Sensor. A small portion of the light tunnels through the near-field aperture

and is used for near-field optical microscopy. Distance control between tip and sample is done using the well known beam-deflection principle (Fig. 2.9).

A second laser with different wavelength is focussed onto the cantilever and the reflected signal is detected with a segmented photodiode. The force on the sample is proportional to the bending of the cantilever. If the bending of the cantilever changes, the position of the laser beam on the photodiode changes accordingly. This position change is registered by the electronics and is used to correct for the vertical position of the sample. The feedback electronic tries to hold the bending of the cantilever (and therefore the force onto the sample) constant during the scan.

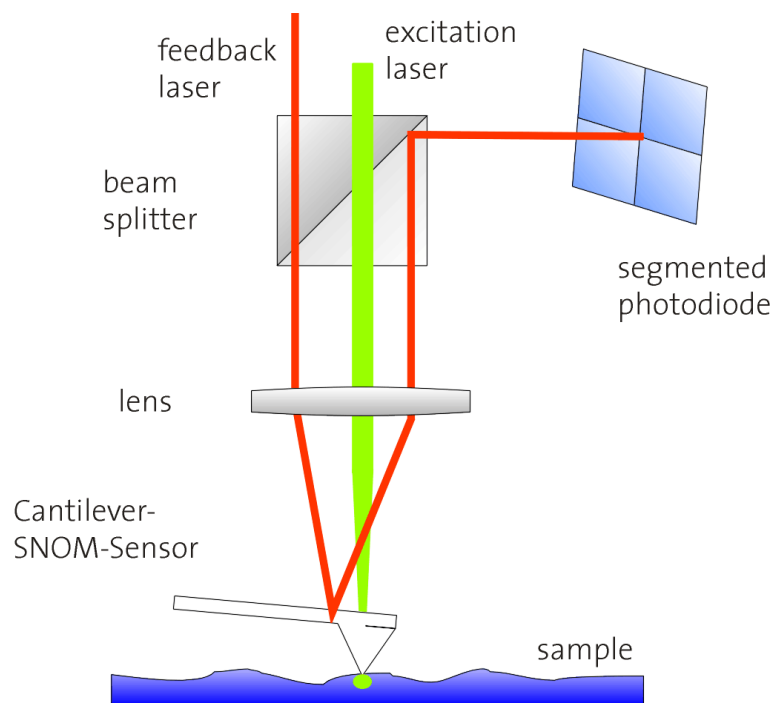


fig. 2.9: Distance feedback with Cantilever-SNOM sensors. The excitation (green) as well as the feedback laser (red) are focussed onto the cantilever through the same lens system. The cantilever is moved into the optical axis of the microscope with a high precision XY-stage for maximum throughput.

Chapter 3

Sample systems

3.1 Reflection at a mirror

Even with relatively cheap microscope objectives, diffraction limited resolution can be obtained if one uses a monochromatic light source (laser) and the objective is only used on-axis. More expensive objectives might have a high chromatic correction for a broad wavelength range, a large planar field of view, a long working distance (large lenses), a good correction in the UV (or IR), a correction ring for different cover glasses or the use in different immersion media or even a combination of several of these features. To achieve diffraction limited resolution it is important to use an objective according to its specifications. Apart from the magnification and the numerical aperture, one can usually find three additional labels printed on the objective. The tube length they are corrected for, cover glass correction and immersion medium, if the objective is corrected for the use in an immersion fluid. Sometimes, also the working distance is indicated and some objectives have an adjustable ring to correct for different cover glass thicknesses. If an objective is used in a wrong beam path, where only one of the parameters differs from the correct value, wave-front errors are introduced that reduce the resolution.

A simple possibility to check the depth resolution in a confocal system is to scan a mirror axial through the focus and record the intensity on the detector. If the beam path is correct, a nearly symmetrical intensity curve with small side maxima can be seen. In addition, the FWHM of the central maximum can be compared to the

theoretical values of section 1.5.2.

Fig. 3.1 shows a typical measurement. The objective (Nikon) is an oil-immersion objective with a numerical aperture of 1,4, corrected for a tube length of 160 mm. Due to the fact that the WITec AlphaSNOM requires objectives that are corrected for a parallel beam path (infinity corrected), an extreme loss in resolution is the consequence.

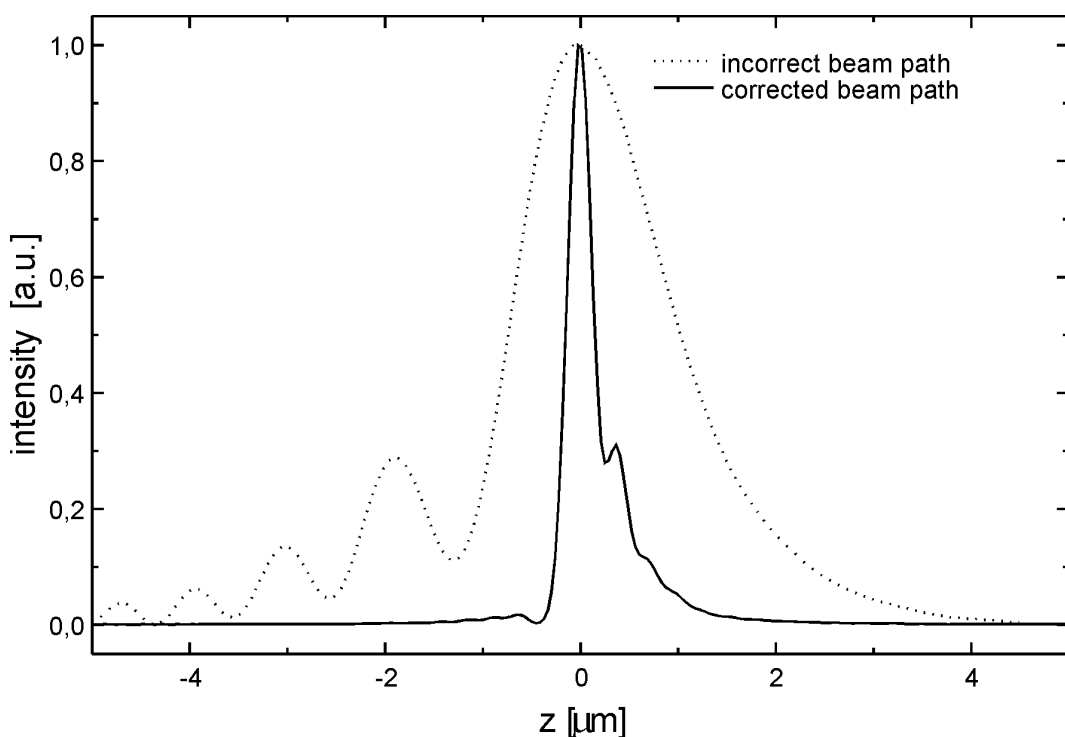


fig. 3.1: Wavefront error due to incorrect beam path, objective: Nikon 100 × \1.4 160 \ 0.17,
 $\lambda = 440 \text{ nm}$.

From the dotted curve in Fig. 3.1, one finds a FWHM of 1770 nm, 6 times higher than the theoretical resolution of this objective of 298 nm. If the objective is used correctly, a FWHM of only 303 nm is obtained, very close to the theoretical value. The reason for the asymmetrical shape is caused by a slightly wrong cover glass thickness used in the experiment.

Fig. 3.2 shows the same experiment without cover glass, but with the correct tube length. If no cover glass is used, the oscillations on the right side are getting stronger and the width increases to 434 nm. From this one can expect that the shoulder completely vanishes, if the correct cover glass thickness of 170 μm is used.

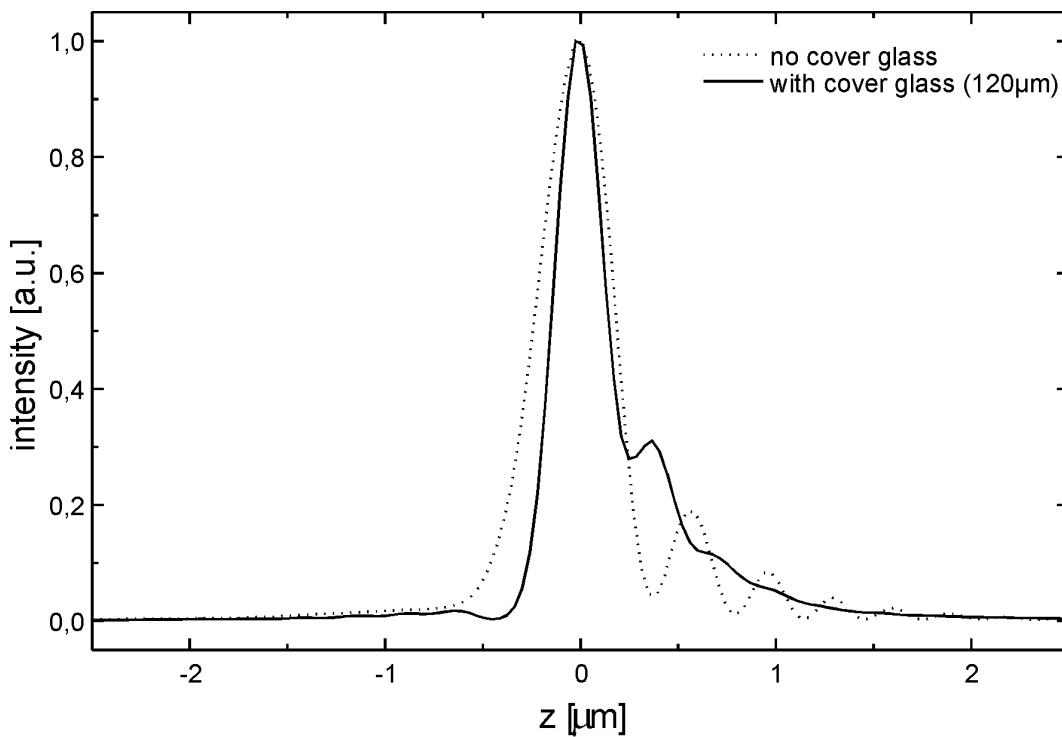


fig. 3.2: Wavefront error due to wrong cover glass thickness, objective: Nikon 100 \times \ 1.4 \ 160 \ 0.17, $\lambda = 440\text{ nm}$.

This behavior can be easily observed, if an objective with variable cover glass correction is used. In this case one can see oscillations on the left or right side of the curve, depending on whether the correction is shifted to smaller or larger values than the correct one.

If the position of the pinhole is laterally shifted relative to the optimum position, a different curve is obtained. Now a minimum can be found at the former position of the maximum (Fig. 3.3). This behavior is observed, if the pinhole is at the position of a minimum of the Airy-pattern, when the mirror surface moves through the focus plane (see Fig. 1.4).

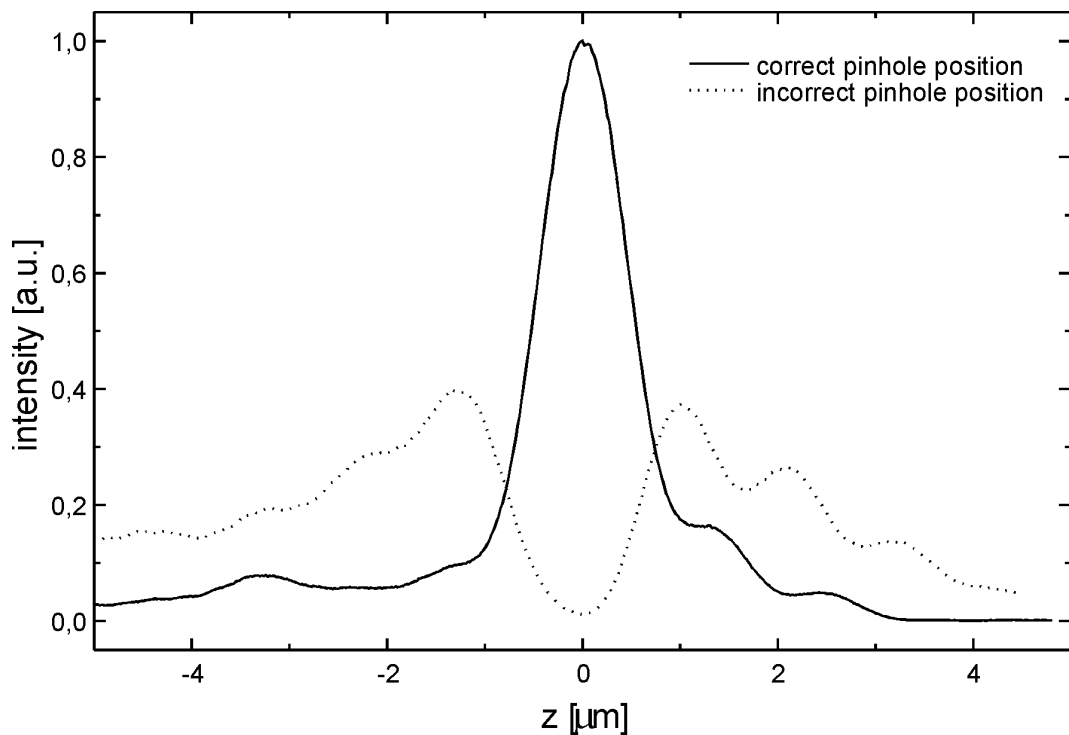


fig. 3.3: Laterally shifted pinhole, objective: Olympus $60 \times \backslash 0.7\infty \backslash 0 - 1.2$, $\lambda = 543 \text{ nm}$.

Fig. 3.4 shows the axial resolution of another objective. The theoretical curve in this diagram was calculated with the point spread function (PSF) for small aperture angles. From this a FWHM of 597 nm was derived, whereas the experiment shows an error of only 6%. One also sees that the height, as well as the position of the side minima is not in complete agreement with theory. Partly, this is due to the fact that $\text{NA}=0.9$ is not a small aperture any more and the theory for large aperture angles has to be used (section 1.3.1). But even small imaging errors, which can be found in any objective, can also lead to this errors. The design of a microscope objective is always a compromise, but many commercial objectives come very close to theory (at least on-axis).

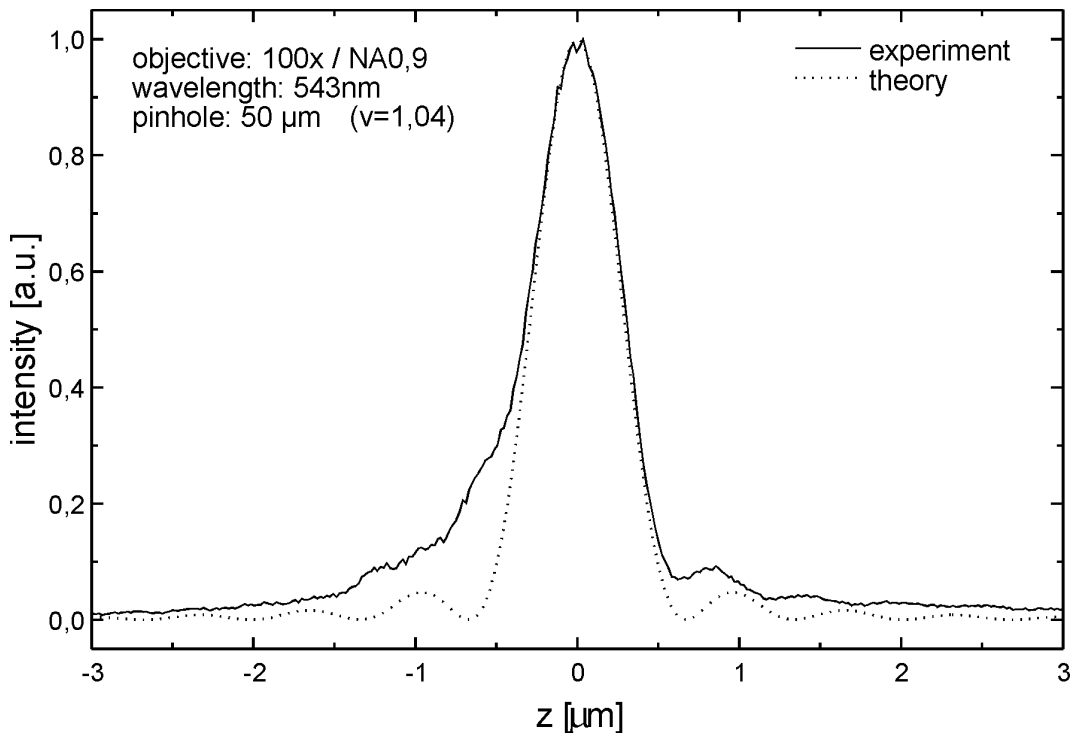


fig. 3.4: Comparison with theory, objective: Olympus 100 \times \ 0.9 ∞ \ 0, $\lambda = 543\text{ nm}$.

3.2 2-photon microscopy

In this section, a water-in-oil emulsion is used as a 3D-model system for 2-photon excitation. A hydrophilic dye (Biocytin Cascade Blue) was used to label the water phase for 2-photon excitation. The absorption maximum of Biocytin Cascade Blue is at 400 nm , the emission maximum at 417 nm .

For the experiment the sample was prepared between two cover slips, so that an oil-immersion objective could be used (Zeiss Neofluar 63x, NA=1,25). The thickness of the sample was around $10\text{ }\mu\text{m}$. The excitation was done with the setup described in section 2.2.4 and the prechirp setup described in section 2.2.5. The Ti:Sapphire laser was used at 780 nm so that the dye was excited at 390 nm , close to its absorption maximum.

It should be noted that the detection in a 2-photon excitation setup is very easy. The excitation wavelength (780 nm) is far from the fluorescence (maximum at 417 nm). Therefore, the filter usually necessary to block the excitation wavelength does not

reduce the detected signal. If only depth resolution and image contrast is important and not the slight increase in resolution which is possible with an extremely small pinhole, a relatively large pinhole can be used. As described in section 1.4.4, the depth resolution in 2-photon microscopy is mainly due to the nonlinear fluorescence generation.

In Fig. 3.5 one can see that the sample consists of water droplets in an oil-phase, as expected for a water-in-oil emulsion. At the position of the dotted line an X-Z scan was performed, which is shown in the lower image. This is a vertical "cut" through the sample. From this one can see that the depth resolution is quite good (below $1\text{ }\mu\text{m}$). The dashed line in the X-Z scan shows the plane of focus in the upper image. Interesting in the depth scan are the vertical filaments that are due to the image formation process. In the same way as clouds the emulsion appears white, because it consists of droplets (water). These droplets act as small lenses because their index of refraction ($n_{\text{water}} \approx 1,33$) is different from the index of the surrounding oil ($n_{\text{oil}} \approx 1,5$). These micro lenses destroy the wavefront of the focus, so that the resolution a few microns below a droplet is strongly reduced.

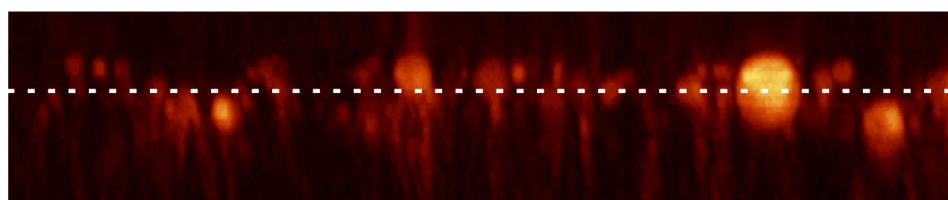
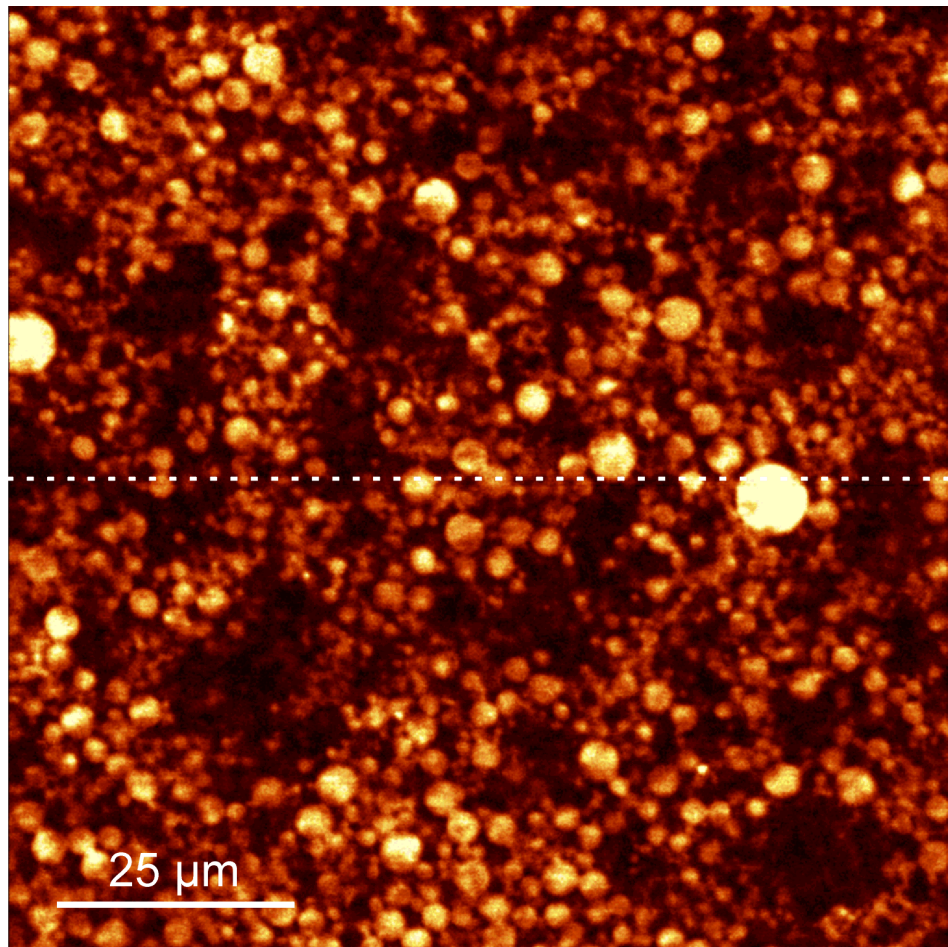


fig. 3.5: 2-photon excitation image of a water-in-oil emulsion ($100 \mu m \times 100 \mu m$),
lower image: vertical cross section (X-Z scan) ($100 \mu m \times 20 \mu m$).

3.3 Confocal fluorescence microscopy

To test and demonstrate the resolution of a confocal microscope, one needs a small and defined fluorescing sample. One possible sample would be a small, labelled latex sphere or even a single molecule.

The problem with this kind of samples, especially if one wants to use an extremely small pinhole for highest resolution ($v_p < 0,5$), is their instability due to photo bleaching. If the excitation intensity has to be chosen too small to get a good signal, the data get very noisy due to photon statistics.

If the single fluorescence photons are independent from each other, the so called Poisson-statistic is valid

$$w_m = \frac{\bar{n}^m}{m!} e^{-\bar{n}} . \quad (3.1)$$

The Poisson-statistic indicates the possibility w_m to measure m photons, if the average value is \bar{n} . The variance σ of this distribution, which is a measure for the uncertainty of a single measurement, can be derived from the mean value:

$$\sigma = \sqrt{\bar{n}} .$$

If, for instance, the mean value is 300 *photons*, the uncertainty of a single measurement is 17 *photons* (6%). To get a good statistics, a high number of photons has to be counted to get a smaller error (the absolute error gets larger, but the percentage of the error gets smaller).

For most fluorescing samples one has to make a compromise between highest resolution (small pinhole) and high signal (Fig. 2.5). Therefore, in most confocal microscopes the pinhole size is adjustable and most of the time they are operated with a moderate pinhole diameter. This usually reduces the resolution to that of a conventional microscope, but still preserves a high contrast and a good depth resolution.

To demonstrate the possible resolution, a thick layer of fluorescent labelled latex spheres (48 nm) was prepared. After the layer dried, small cracks appeared.

Fig. 3.6 shows a fluorescence image and a magnified detail. The small cracks that run perpendicular to the large ones have a typical width of below 200 nm. A cross section through such a crack is shown in Fig. 3.7.

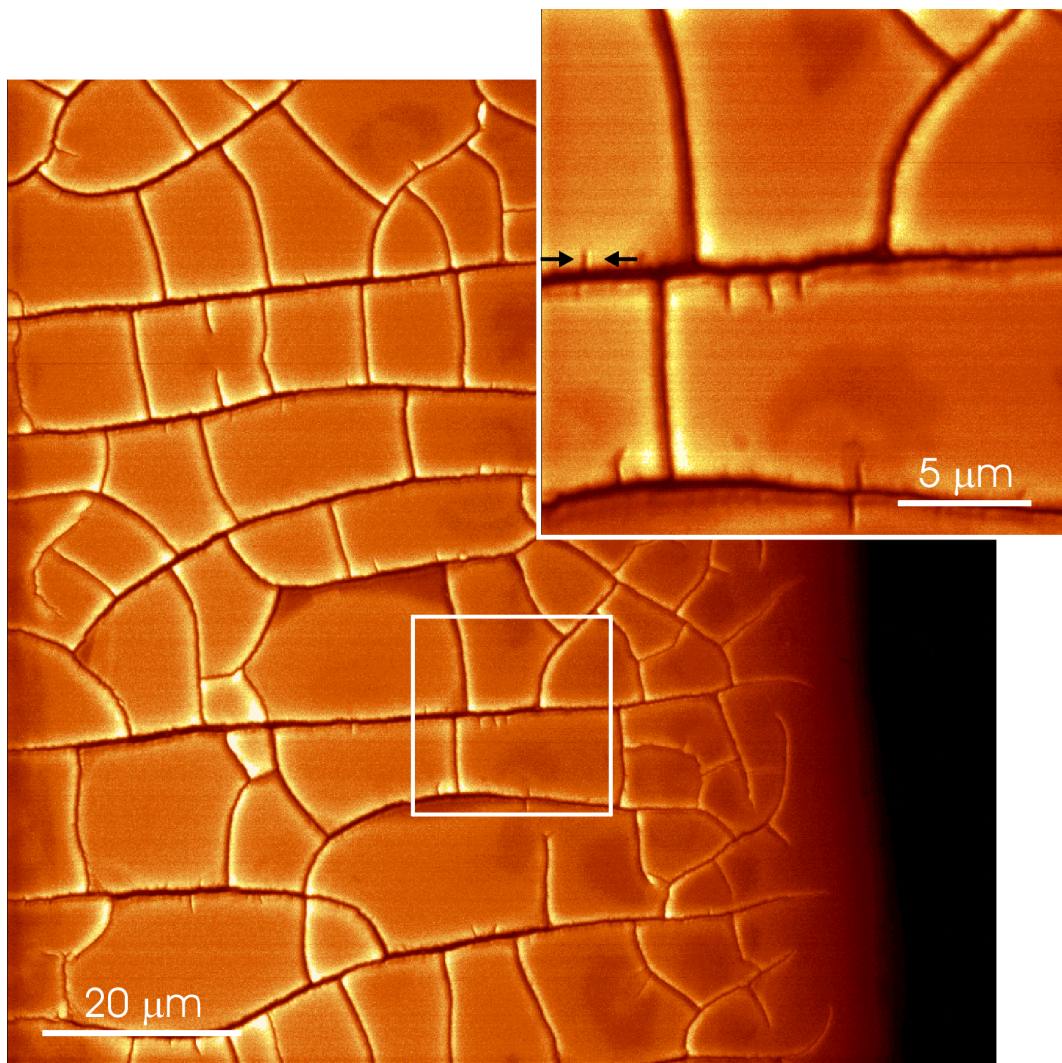


fig. 3.6: Dried layer of fluorescing latex spheres with cracks

A small uncertainty is the determination of the background signal (dotted line), because the stray light background is different on both sides of the minimum. If one assumes the curve in Fig. 3.6 to be precise, the FWHM is between 160 nm and 180 nm , due to the different background on both sides. If one adds the uncertainty due to the Poisson-statistic, these values have an additional error of about 10%.

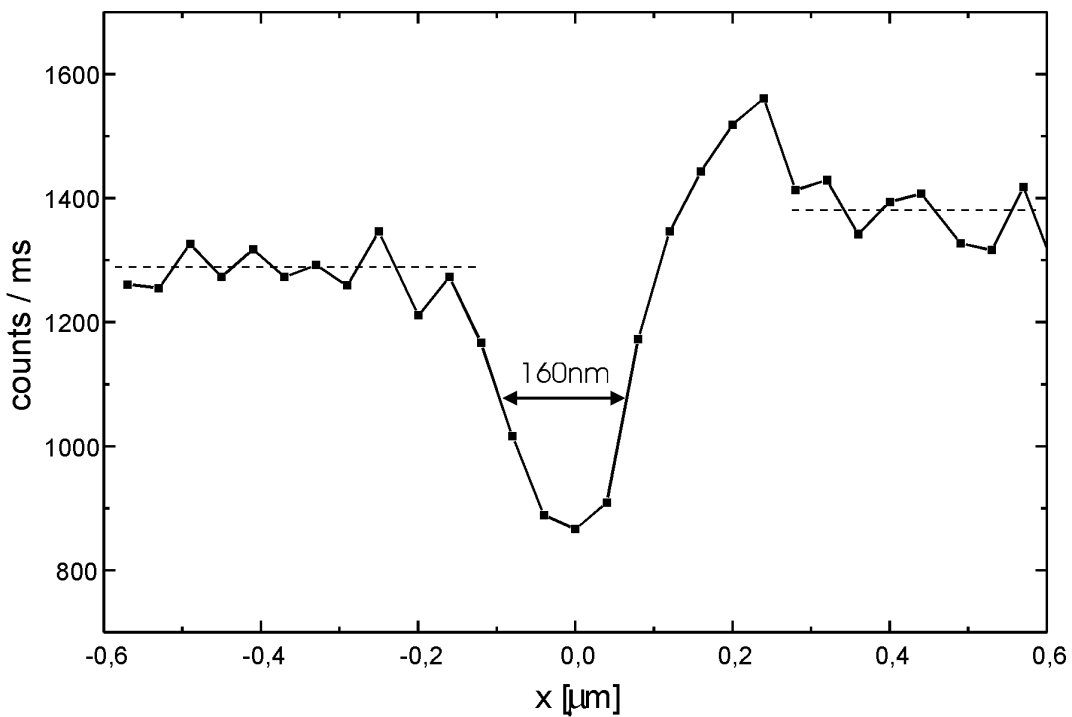


fig. 3.7: Cross section through the crack in Fig. 3.6

With the values from Tab. 3.1 one gets a theoretically possible resolution for the confocal image of 142 nm.

excitation wavelength	440 nm
absorption maximum	458 nm
emission maximum	540 nm
filter	GG 495
objective	63 × /1, 25 ∞/0, 17 Öl
pinhole	2, 4 μm ($v_p = 0, 33$)

Tab. 3.1: Technical data for the measurement in Fig. 3.6.

If one takes the average value of 170 nm for the experimentally realized resolution, the theoretical limit is missed by only 28 nm, but one has to pay a high price for this resolution. Due to the extremely small pinhole ($v_p = 0, 33$) the detected fluo-

cence is only a few percent of the signal that would be detected without pinhole. There are several possible reasons for the discrepancy between theoretical and experimental resolution. This can be due to the sample itself, due to the theoretical model behind the calculation of the width or due to deficits in the optics. Most likely it is due to the sample. If, e.g. the thickness of the crack is not extremely small, it can not be neglected any more and the FWHM will be larger than the theoretical limit.

To summarize, one can see that the theoretical resolution of a conventional microscope with point like excitation of 182 nm was improved with confocal detection by at least 12 nm . This improvement is small, but the wavelength difference between excitation and detection was quite large (100 nm). Only if this difference vanishes, the confocal detection can produce a gain in resolution that is worth mentioning. On the other hand, if the gain in resolution is compared to conventional microscopy without point like excitation (photo or view through binocular), the gain is much larger. In this case, the maximum resolution is only 223 nm , because the fluorescence wavelength determines the resolution.

3.4 Confocal versus near-field microscopy

Not in all cases a resolution of below 200 nm can be obtained with conventional microscopy. The results in the last paragraph were obtained under nearly ideal conditions: excitation with blue light, observation with an oil immersion objective and confocal detection. If e.g. a sample has to be observed in air, the excitation must be done with green light and one can not use an extremely small pinhole, the resolution will be less than 300 nm . The only way to increase the resolution is then to use a near-field probe.

In this section, a conventional laser-scanning image is compared with a near-field optical image, obtained at the same sample position. The sample used for this comparison is a latex projection pattern, a glass substrate with small aluminium islands. The sample was prepared as follows. In a first step, a monolayer of latex spheres with 450 nm diameter was deposited on a glass substrate. A very thin aluminium layer $12 - 15\text{ nm}$ was then evaporated onto this structure. After this, the latex spheres were removed.

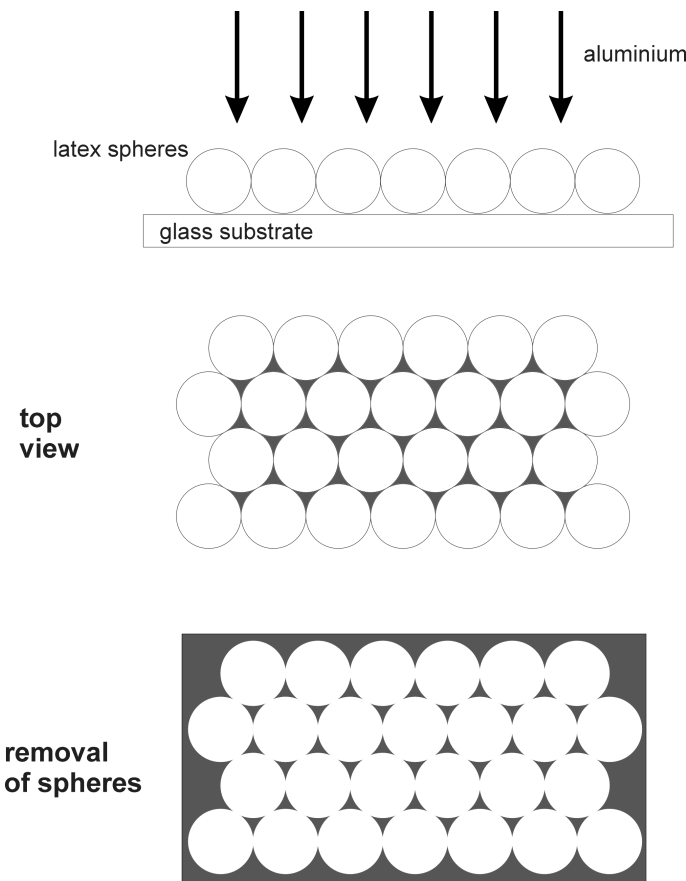


fig. 3.8: A latex projection pattern is a simple test structure for probing the resolution of a microscope. A mono-layer of latex spheres is deposited on a glass substrate. Then, a thin layer of aluminium is evaporated on top and the latex spheres are removed.

The aluminium forms a hexagonal structure of small islands, separated by about 225 nm. This sample is an ideal test structure to determine resolution in the imaging setup.

Fig. 3.9 shows an overview, as well as two close-up images obtained by conventional microscopy in transmission. The image was acquired with a 100x, NA=0,9 objective in air at an excitation wavelength of 532 nm. Fig. 3.10 shows the same areas, obtained with a near-field optical setup with cantilever sensors at the same excitation wavelength.

The resolution in the conventional image of about 350 nm is determined by the diameter of the excitation spot. If a confocal detection with an extremely small pin-hole ($v_P < 0,5$) diameter would have been used, the resolution would be 250 nm . The resolution in the near-field images is independent of the excitation wavelength and only determined by the diameter of the near-field aperture. In this case, the aperture was around 80 nm ($\frac{\lambda}{7}$).

Not in all cases the improvement achieved by near-field microscopy is so impressive as in this case. The ideal sample for conventional microscopy is embedded in immersion liquid (e.g. oil or water) and can be excited in the blue (or even the UV). In this case ($N_A = 1,4$, $\lambda = 440\text{ nm}$) and under perfect conditions, a theoretical resolution of 135 nm can be obtained. On the other hand, an ideal sample for near-field microscopy has to be investigated in air in the green or red (or even better in the IR) part of the spectrum. In this case, the gain in resolution compared to conventional microscopy is very impressive. If e.g. a wavelength of 700 nm has to be used, the best resolution for a confocal setup would be 330 nm , for a conventional setup only 470 nm . If this is compared to the 80 nm resolution routinely achieved with a near-field microscope, the improvement is remarkable (factor of 4 compared to confocal, factor of 6 compared to conventional microscopy).

Depending on sample and aperture, even higher resolutions are possible with a near-field optical microscope. Fig. 3.11 shows a $2\text{ }\mu\text{m} \times 2\text{ }\mu\text{m}$ scan of the same kind of sample with a cross section showing a resolution of 29 nm obtained with 532 nm excitation ($\frac{\lambda}{18}$)!

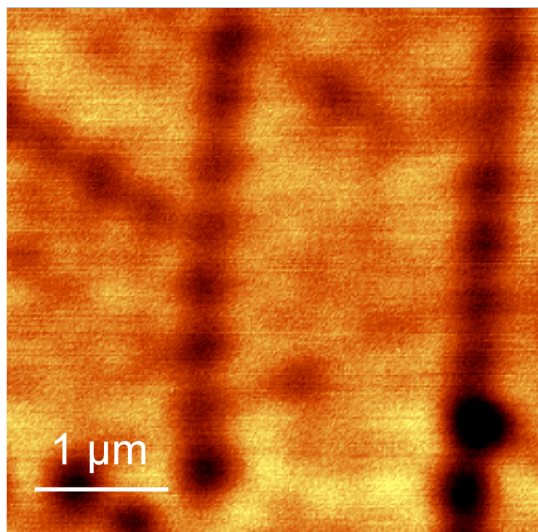
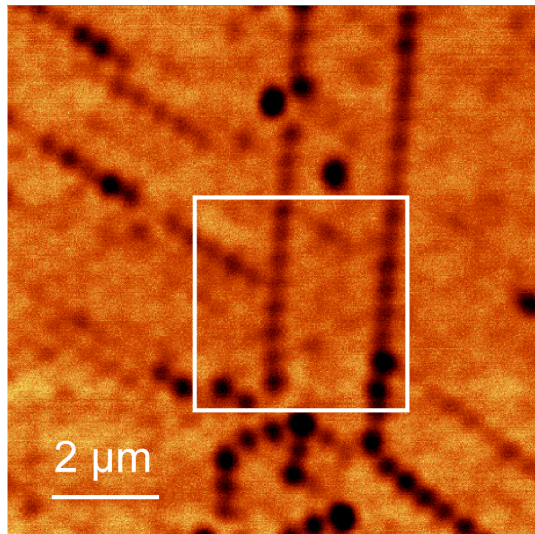
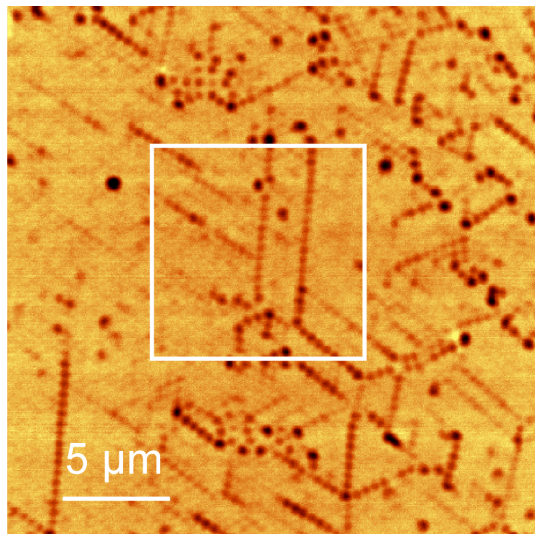


fig. 3.9: Resolution of a conventional microscope with green laser excitation (532 nm). The image was obtained with a 100x, NA=0,9 objective in transmission. Sample: latex projection pattern with 450 nm latex spheres. The resolution in the images is about 350nm.

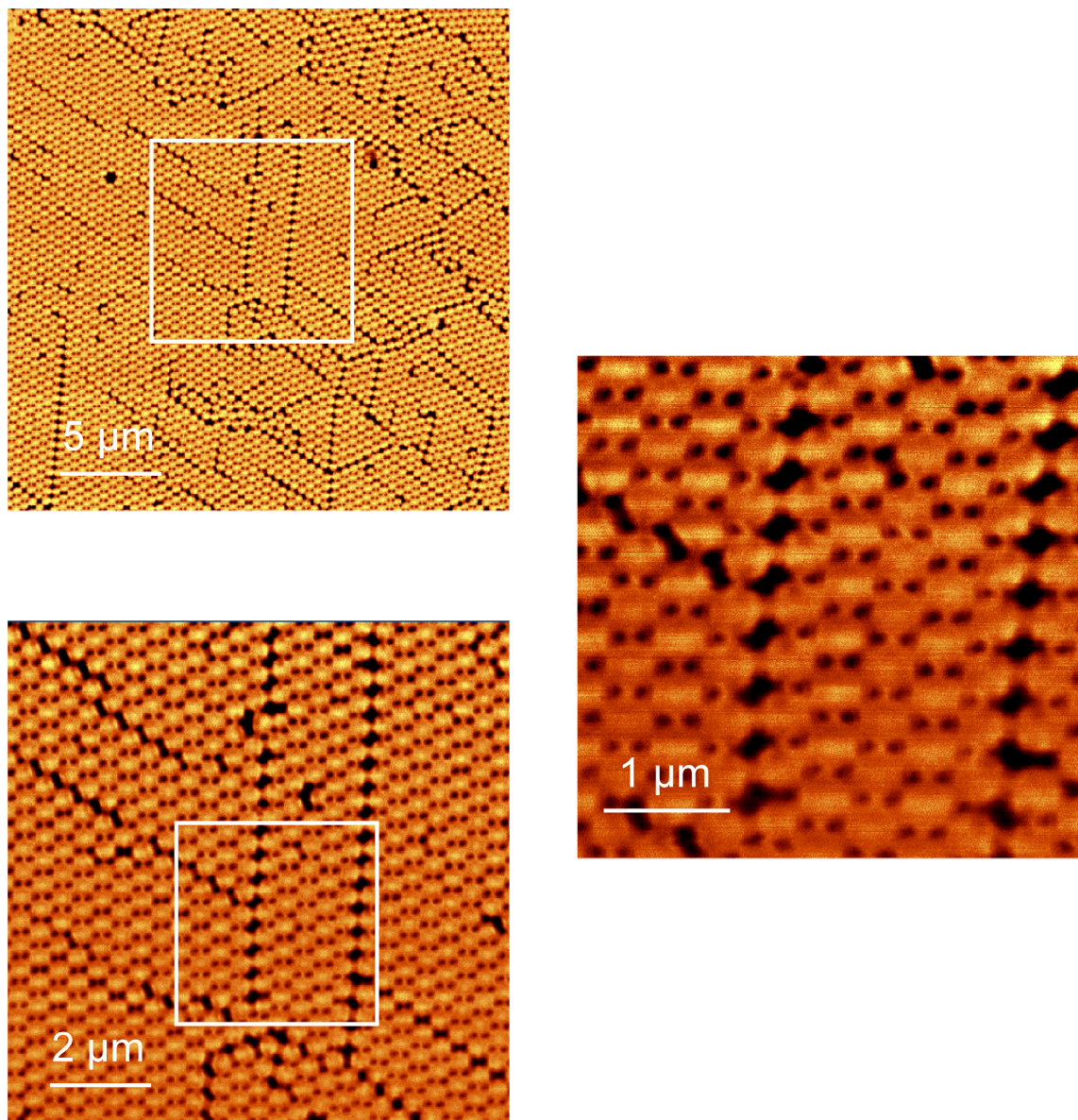


fig. 3.10: Overview (top) and two close-up images obtained with a 80 nm SNOM aperture in transmission. The images show the same areas as in Fig. 3.9.

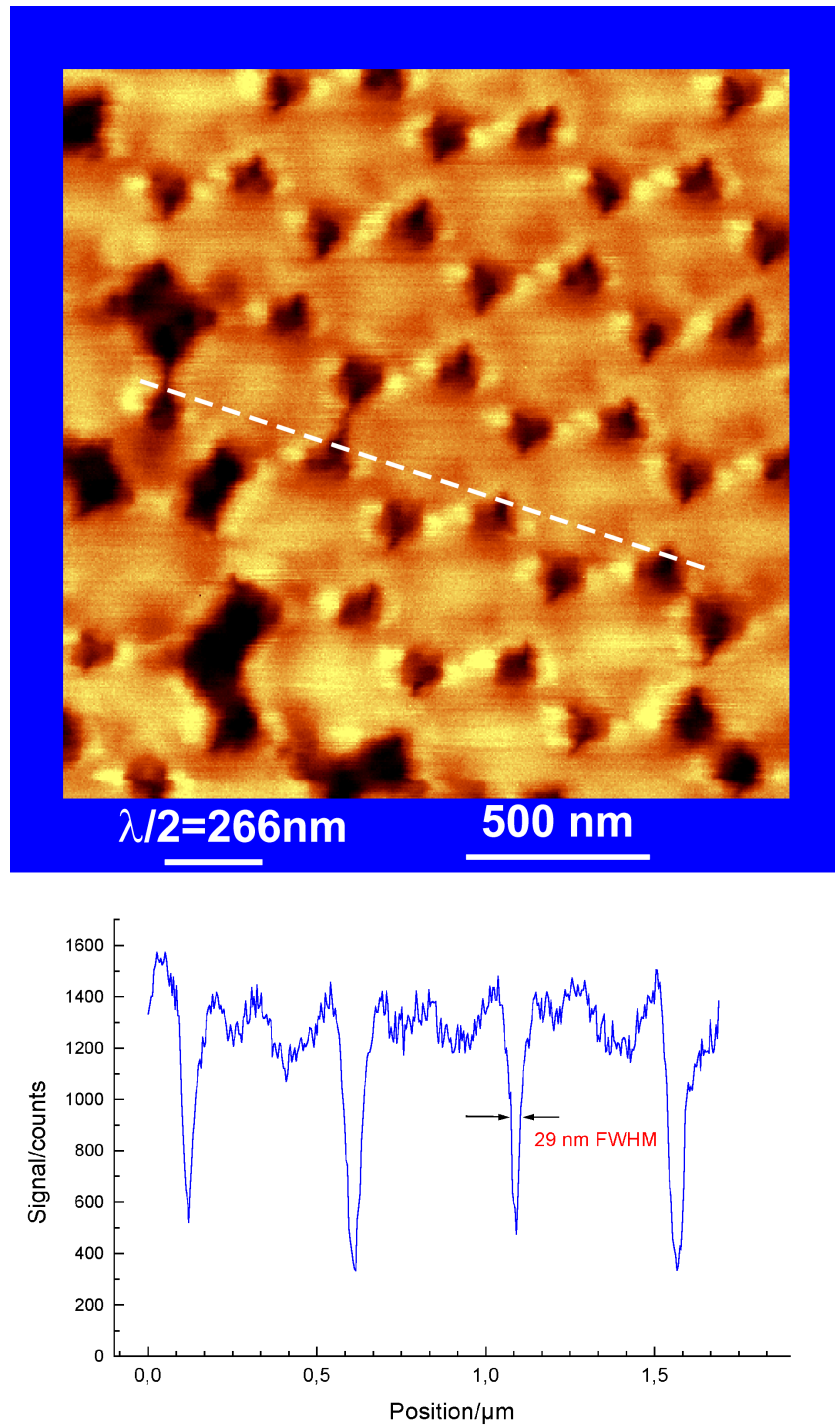


fig. 3.11: $2\text{ }\mu\text{m} \times 2\text{ }\mu\text{m}$ near-field scan of a latex projection pattern (Fig. 3.8) with an extremely small aperture. The cross section shows a resolution (FWHM) of below 30nm ($\frac{\lambda}{18}$).

3.5 Depth resolution in confocal fluorescence microscopy

In Fig. 3.13 a confocal fluorescence image of perylene tetracarboxylic acid bisimide dyes¹ and melamines are shown. Between both substances, hydrogen-bonded supramolecular chains are formed (Fig. 3.12) that cluster to densely intertwined networks of nano- to mesoscopic strands.

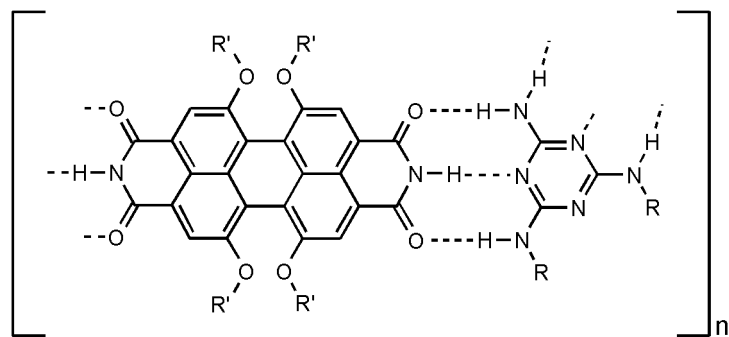


fig. 3.12: Chemical structure of perylene tetracarboxylic acid bisimide and melamine, which form supramolecular chains with hydrogen bonds.

With a transmission electron microscope (TEM), this structure has been imaged before, but only with a fluorescence microscope it could be confirmed that perylene tetracarboxylic acid bisimide dyes were incorporated into these chains.

Fig. 3.13 shows this interesting network structure after excitation with a green He-Ne laser (543 nm).

¹The samples have been prepared in the Abteilung Organische Chemie II at the Universität Ulm, Germany (F. Würthner, C. Thalacker und A. Sautter).

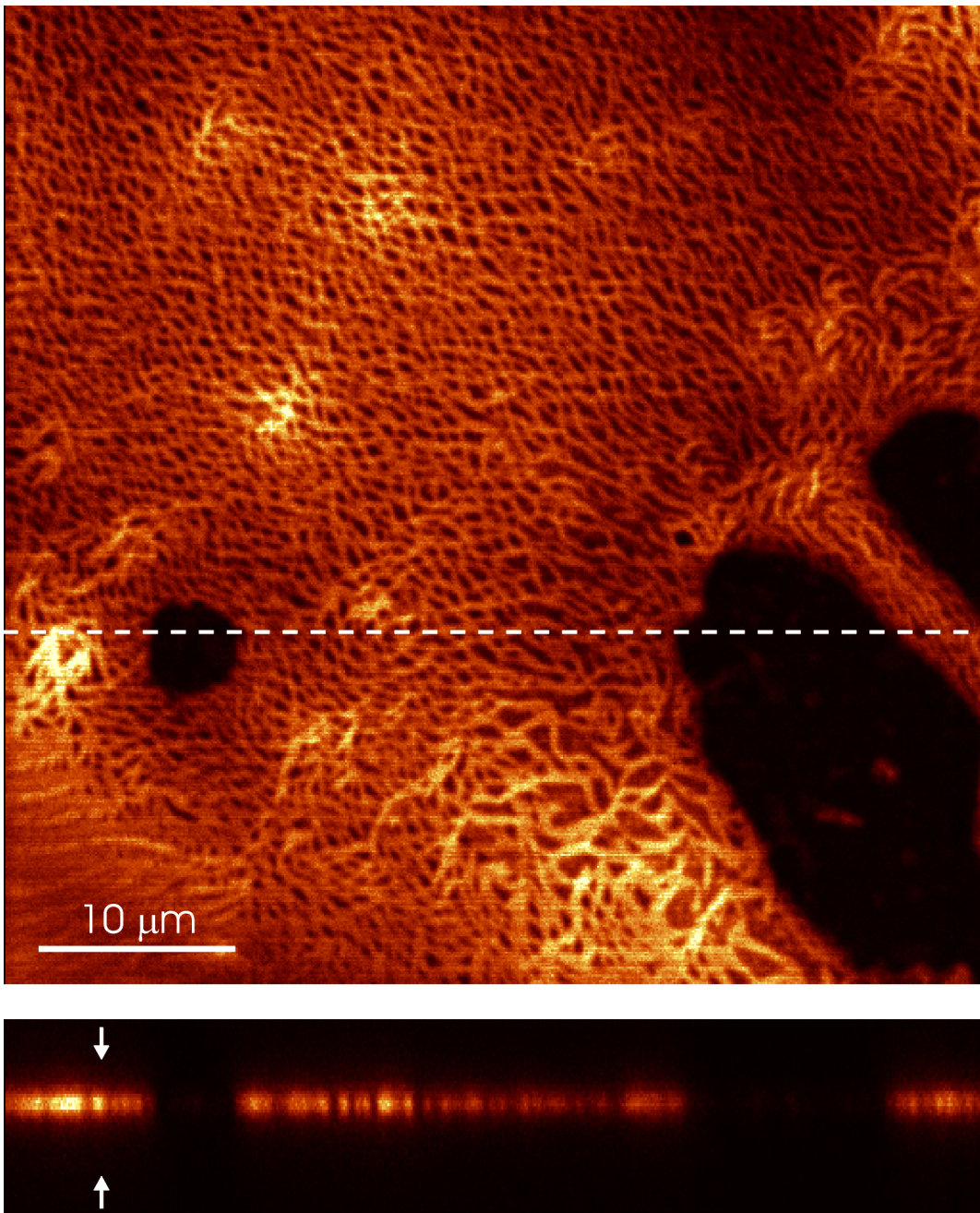


fig. 3.13: Confocal fluorescence image. Top: Self organized perylene tetracarboxylic acid bisimide-melamine chains. Bottom: Axial cut along the dashed line. Arrows: see Fig. 3.14.

A $10 \mu\text{m}$ deep confocal cut through the sample (dashed line) can be seen, which can be used to determine the axial resolution for this setup. If the fluorescing layer is

vertically moved through the focus, a typical intensity profile as shown in Fig. 3.14 is obtained. From the values in Tab. 3.2 and Fig. 1.13 one calculates a depth resolution of 780 nm .

excitation wavelength	543 nm
emission maximum	596 nm
filter	OG 590 ($\beta \approx 1,2$)
objektive	$63 \times /1,25 \quad \infty/0,17\text{ Öl}$
Pinhole	$25\text{ }\mu\text{m}$ ($v_p = 2,8$)

Tab. 3.2: Technical data for the measurement of Fig. 3.13.

The resolution achieved in the experiment is only 1090 nm . In addition to the wave-front errors (due to wrong cover slip thickness, beam-splitter, lenses etc.) discussed in section 3.3 another problem crops up. Using an immersion-objective it is important that the medium surrounding the sample has the same index of refraction than the immersion-oil itself. The enhanced resolution of an immersion objective is due to the fact that the wavelength of light in a medium is reduced by the factor of the refractive index of this medium. In the experiment, the sample was at the bottom surface of a cover slip while observed through the immersion oil and the cover slip. Due to the fact that the sample is at the interface of air and glass, it is optically seen half in air and half in glass. Therefore the effective index of refraction is somewhere between $n = 1$ and $n = 1,5$. If one assumes the effective index to be $n = 1,25$, the theoretical resolution is reduced to 940 nm and the discrepancy between theory and experiment reduces to 15%. As another point, the sample has also a finite thickness which can easily explain the remaining difference.

This approach might be too simple to explain the experiment in detail, but it demonstrates that for optimum results the sample has to be fully immersed in an appropriate medium. For the imaging of biological cells, mostly water-immersion objectives are used that can be directly dipped into the physiological solution.

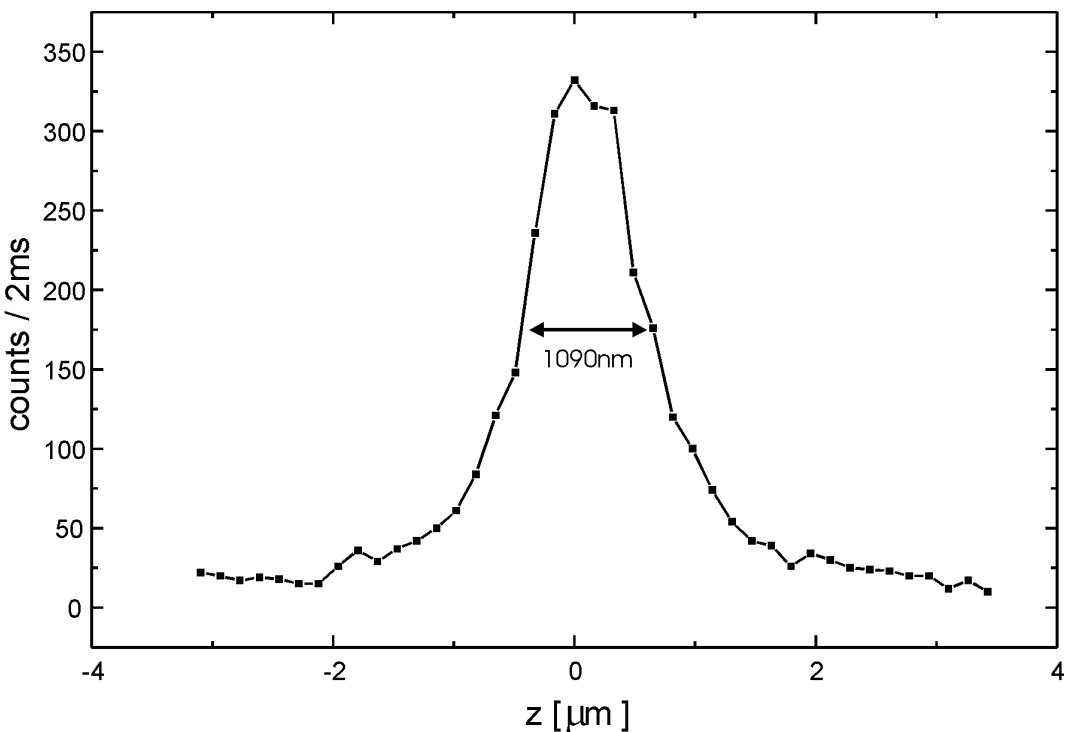


fig. 3.14: Intensity profile of the line in Fig. 3.13 marked with the arrows.

3.6 Imaging of a semiconductor surface

One problem in conventional microscopy is that if objects with relatively high topography (like biological cells or structured semiconductors) are observed, also plains out of focus contribute to the final image. In confocal microscopy, only the areas in the focal plane contribute to the image, so that the image is always focussed. If an object is moved through focus, it vanishes when it gets out of focus. Therefore, if many of these images are obtained at different focal planes, a 3D-image of the sample can be obtained. This stack of images can be visualized in different ways. From simple cuts to projections, complicated 3D-images or even animated flights over the sample can be calculated with modern computation power. In the following, two simple evaluation methods will be described, which are well suited to the imaging of reflecting surfaces.

3.6.1 Extended focus

Single images of this stack might look very strange, because each image contains only information of a certain sample plane. Small details, but even large area connections might be hidden in the individual image, especially if the sample is a little bit tilted with respect to the scanning plane. A first overview can be obtained by simply adding up all single images

$$I(x_0, y_0) = \sum_{i=1}^n I(x_0, y_0, z_i) \quad .$$

Such a presentation is called an extended focus image (Fig. 3.15).

Fig. 3.16 shows a structured semiconductor surface (German telephone card chip). The upper image is one single images, while the lower image is the sum of all 51 images of this stack. The advantage of this extended focus image is that the entire image is always in focus, even for samples with very high topography.

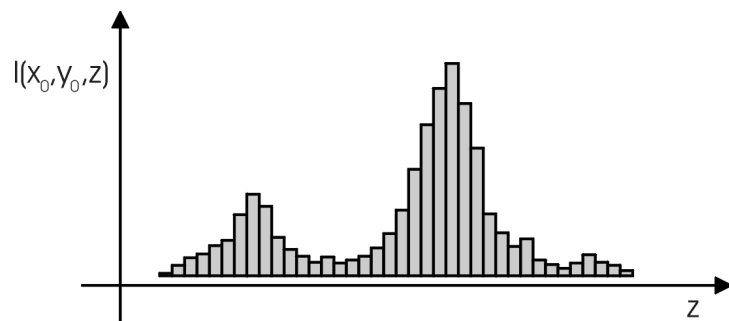


fig. 3.15: Scheme to calculate extended focus images.

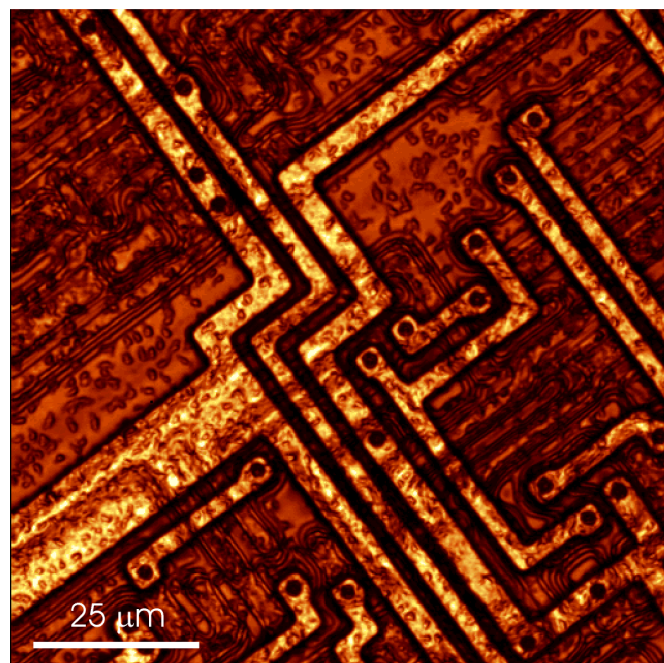
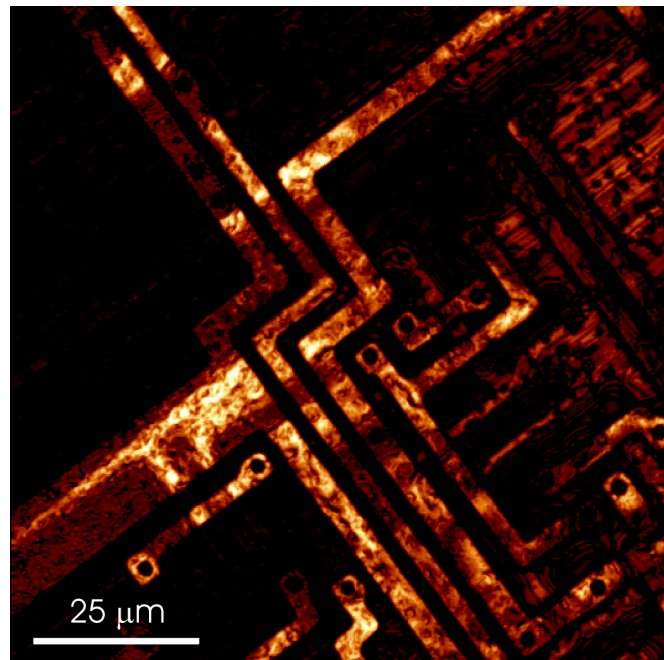


fig. 3.16: Extended focus of a structured semiconductor surface (German telephone card chip), top: single image, bottom: extended focus image.

3.6.2 Automatical focus

Using the method of automatical focus, one gets the reflectivity of the sample as well as the topography.

In the automatical focus method one looks for the maximum signal at every image pixel (Fig. 3.17). The position of the maximum (z_{max}) gives information about the topography, the intensity itself ($I(x_0, y_0, z_{max})$) is determined by the reflectivity of the surface. This method delivers a combined image of topography and reflectivity. A disadvantage is that the information of a second maximum (a small detail in front or behind strong emitting objects of a transparent sample) in the reflectivity is completely lost after image calculation.

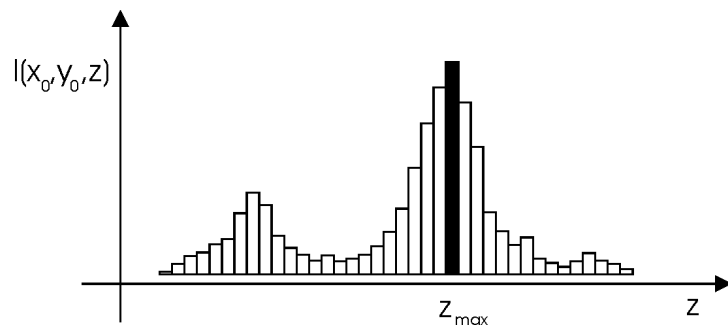


fig. 3.17: Scheme to calculate extended focus images.

Fig. 3.18 shows the same stack of 51 images of a semiconductor surface. The focus distance for each image was 200 nm. The information for topography (z-position of maximum reflectivity) and reflectivity can be combined in a single 3D-presentation.

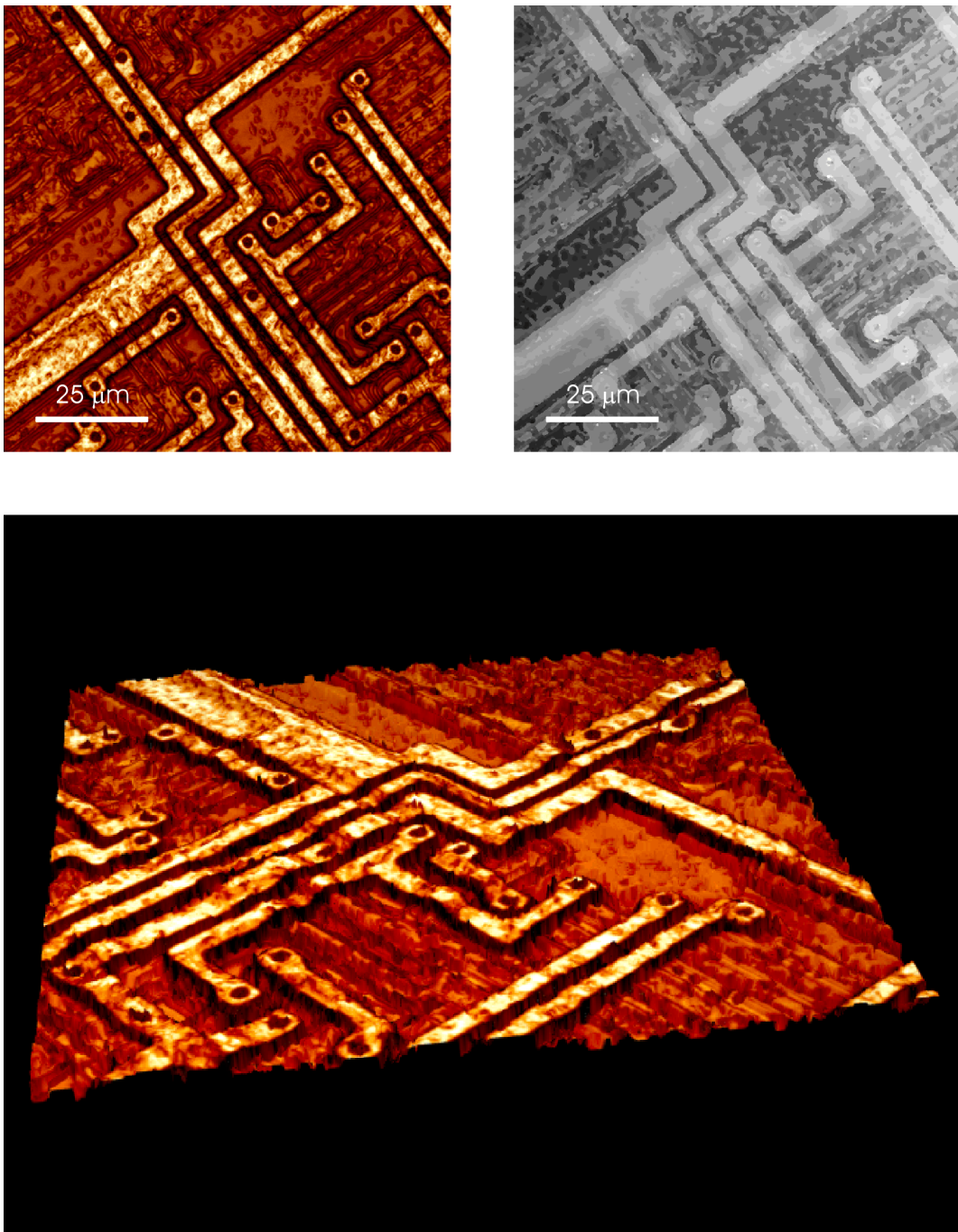


fig. 3.18: Structured semiconductor, top left: automatical focus, top right: topography (every different color represents a height difference of 200 nm), below: combined 3D-representation of both images. The maximum topography in the image is 4,8 μm .

Bibliography

- [1] James B. Pawley. Handbook of biological confocal microscopy. Plenum Press, 2. edition, 1995.
- [2] E. Wolf. Electromagnetic diffraction in optical systems, Part I. *Proc. R. Soc. London*, **A 253**:358–379, 1959.
- [3] E. Wolf. A Scalar Representation of Electromagnetic Fields, Part II. *Proc. Phys. Soc.*, **74**:269–280, 1959.
- [4] B. Richards and E. Wolf. Electromagnetic diffraction in optical systems, Part II. *Proc. R. Soc. London*, **A 253**:358–379, 1959.
- [5] R. Juškaitis and T. Wilson. The measurement of the amplitude point spread function of microscope objective lenses. *Journal of Microscopy*, **189**:8–11, January 1998.
- [6] T. Wilson. Confocal Microscopy, chap. IV.2. The imaging of simple objects, pp. 25–30. Academic Press, 1990.
- [7] T. Wilson. Confocal Microscopy, chap. IV.2. The imaging of simple objects, pp. 41–45. Academic Press, 1990.
- [8] C. J. R. Sheppard and M. Gu. Image formation in two-photon fluorescence microscopy. *Optik*, **86(3)**:104, 1990.
- [9] M. Gu and C. J. R. Sheppard. Comparison of three-dimensional imaging properties between two-photon and single-photon fluorescence microscopy. *J. Microsc.*, **177**:128–137, 1995.

- [10] M. Gu and C. J. R. Sheppard. Effects of a finite sized pinhole on 3D image formation in confocal two-photon fluorescence microscopy. *J. Mod. Opt.*, **40**:2009–2024, 1993.
- [11] T. Wilson and A. R. Carlini. Size of the detector in confocal imaging systems. *Optics Letters*, **12**:227–229, April 1987.
- [12] T. Wilson. Confocal Microscopy, chap. III. Fluorescence imaging, pp. 114–115. Academic Press, 1990.
- [13] S. W. Hell and E. H. K. Stelzer. Properties of a 4Pi-confocal fluorescence microscope. *J. Opt. Soc. Am.*, **A9**:2159–2166, 1992.
- [14] E. H. K. Stelzer and S. Lindek. Fundamental reduction of the observation volume in far-field light microscopy by detection orthogonal to the illumination axis: confocal theta-microscopy. *Opt. Commun.*, **111**:536–547, 1994.
- [15] E. A. Synge. A Suggested Method for extending Microscopic Resolution into the Ultra-Microscopic Region. *Philosophical Magazine*, **6**:356–362, 1928.
- [16] E. A. Ash and G. Nicholls. Super-resolution Aperture Scanning Microscope. *Nature*, **237**:510–512, 1972.
- [17] D. W. Pohl, W. Denk and M. Lanz. Optical stethoscopy: image recording with $\lambda/20$. *Appl. Phys. Lett.*, **44**:651–653, 1984.
- [18] E. Betzig, J. K. Trautman, T. D. Harris, J. S. Weiner and R. L. Kostelak. Breaking the diffraction barrier: optical microscopy on a nanometric scale. *Science*, **257**:1468–1470, 1991.
- [19] A. Harootunian, E. Betzig, M. Isaacson and A. Lewis. Super-resolution fluorescence near-field scanning optical microscopy. *Appl. Phys. Lett.*, **49**:674–676, 1986.
- [20] C. Mihalcea, W. Scholz, S. Werner, S. Mnster, E. Oesterschulze and R. Kassing. Multi-Purpose Sensor Tips for Scanning Nearfield Microscopy. *Appl. Phys. Lett.*, **68(25)**:3531–3533, 1996.

- [21] Michael A. Paesler and Patrick J. Moyer. Nearfield Optics, Theory, Instrumentation and Applications. JOHN WILEY & SONS, INC., 1. edition, 1996.
- [22] J. D. Jackson. Classical Electrodynamics. John Wiley & Sons, New York, 2. edition, 1975.

